Timing and stepwise transitions of the African Humid Period from geochemical proxies in the Nile deep-sea fan sediments

Guillemette Ménot, Sébastien Pivot, Ioanna Bouloubassi, Nina Davtian, Rick Hennekam, Delphine Bosch, Emmanuelle Ducassou, Edouard Bard, Sebastien Migeon, Marie Revel

▶ **To cite this version:**

Guillemette Ménot, Sébastien Pivot, Ioanna Bouloubassi, Nina Davtian, Rick Hennekam, et al.. Timing and stepwise transitions of the African Humid Period from geochemical proxies in the Nile deep-sea fan sediments. Quaternary Science Reviews, 2020, 228, pp.106071. 10.1016/j.quascirev.2019.106071 . hal-02406506

HAL Id: hal-02406506
https://hal.science/hal-02406506

Submitted on 21 Jul 2022

HAL is a multi-disciplinary open access archive for the deposit and dissemination of scientific research documents, whether they are published or not. The documents may come from teaching and research institutions in France or abroad, or from public or private research centers.

L'archive ouverte pluridisciplinaire **HAL**, est destinée au dépôt et à la diffusion de documents scientifiques de niveau recherche, publiés ou non, émanant des établissements d'enseignement et de recherche français ou étrangers, des laboratoires publics ou privés.

Distributed under a Creative Commons Attribution - NonCommercial| 4.0 International License

Version of Record: https://www.sciencedirect.com/science/article/pii/S0277379119305931
Manuscript_ad0d3ab8a0031df8fc1e08f2bcab5750

Timing and stepwise transitions of the African Humid Period from geochemical proxies in the Nile deep-sea fan sediments

Guillemette Ménot [a]*, Sébastien Pivot [b], Ioanna Bouloubassi [c], Nina Davtian [b], Rick Hennekam [d], Delphine Bosch [e], Emmanuelle Ducassou [f], Edouard Bard [b], Sébastien Migeon [g], Marie Revel [g]

a: Univ Lyon, ENS de Lyon, Université Lyon 1, CNRS, UMR 5276 LGL-TPE, F-69364, Lyon, France

b: CEREGE, Aix Marseille Univ, CNRS, IRD, INRA, Collège de France, Technopôle de l'Arbois, BP80, 13545 Aix-en-Provence, France

c: Sorbonne Universités, UPMC Univ Paris 06, CNRS, IRD, MNHN, LOCEAN, 4 place Jussieu, 75252, Paris cedex 05, France

d: NIOZ Royal Netherlands Institute for Sea Research, Department of Ocean Systems, and Utrecht University, P.O. Box 59, 1790 AB Den Burg, Texel, The Netherlands

e: Géosciences Montpellier, Université de Montpellier UMR-CNRS 5243, 34095 Montpellier, France

f: Université de Bordeaux 1, UMR-CNRS 5805-EPOC, allée Geoffroy St Hilaire 33615 Pessac Cedex, France

g: Geoazur, 250 Rue Albert Einstein 06560 Valbonne-Sophia Antipolis, France

*Corresponding author

E-mail address: guillemette.menot@ens-lyon.fr

© 2019 published by Elsevier. This manuscript is made available under the CC BY NC user license
https://creativecommons.org/licenses/by-nc/4.0/

Abstract

Large fluvial systems, such as the Nile River, allow a basin-scale integrated view of climatological and environmental changes. In this study, we reconstructed the Nile discharge history for the last 20 ka using molecular ratios of glycerol dialkyl glycerol tetraethers (GDGTs) and neodymium (Nd) radiogenic isotopes. By characterizing both the organic and inorganic fractions, we assessed the relevance of the GDGT-based proxies in deltaic environments as tracers of terrigenous origin. A large increase in Nile discharge is documented from 14.8 to 8.4 ka BP reflecting enhanced physical erosion and transport processes from the Ethiopian Traps. We confirmed the primary control of insolation on precipitation on North East Africa through the last 20 ka. The centennial time resolution reached on the sedimentary sequence revealed a step-wise onset and termination of the African Humid Period (AHP) starting at 14.8 ka and ending at 8.4 ka BP, respectively. Our centennial-millennial records allowed furthermore pinpointing the abrupt periods of arid conditions corresponding to the Younger Dryas. These data illustrate the linkage between low and high latitude hydrological variability.

Keywords: African Humid Period; Nile River; clastic εNd; GDGT-indices

1. Introduction

African climate varied greatly during the late Quaternary with alternating periods of aridity and humidity (Singarayer and Burrough, 2015). The last major humid phase in Northern Africa, i.e., the African Humid Period (AHP, deMenocal et al., 2000; Shanahan et al., 2015; Tierney et al., 2011), occurred during the early and mid-Holocene (~11–5 ka BP, Gasse, 2000). The development of the so-called "Green Sahara" during the AHP allowed the establishment of large lake systems in Northern Africa and vegetation in areas that are now desert. Human colonization was possible at latitudes 800 km further north than now (Kropelin et al., 2008; Kuper and Kropelin, 2006). This wet African phase has been attributed to the northward migration of the rain belt associated with the Intertropical Convergence Zone (ITCZ) induced by precession-forced insolation changes. These changes started at the end of the Last Glacial Maximum (LGM, Caley et al., 2011; Tuenter et al., 2003). The magnitude of this wet phase was also exemplified by the deposition of the most recent sapropel (S1) in the eastern Mediterranean Sea. Enhanced Nile river runoff led to surface water buoyancy gain, resulting in reduced deep-water ventilation and oxygen deficiency at depth (see Rohling et al., 2015; Rossignol-Strick et al., 1982; Vadsaria et al., 2019).

The termination of the AHP remains highly controversial, albeit frequently studied at many locations in and around the African continent (e.g., Collins et al., 2017; Shanahan et al., 2015; Tierney and deMenocal, 2013). Some studies suggest an abrupt transition that occurred at ~5 ka BP (Collins et al., 2017; deMenocal et al., 2000; McGee et al., 2013; Tierney and deMenocal, 2013). Other studies propose that a gradual AHP termination (Berke et al., 2012; Foerster et al., 2012) or a termination that involved several phases of decreasing humidity (Liu et al., 2017; Loomis et al., 2015). In contrast, the onset of AHP is less controversial and began on the African continent around 15–14 ka (Shanahan et al., 2015; Trauth et al., 2018). However, within the Nile delta, and within the Eastern Mediterranean Sea, there are relatively

few sites with a sufficient time resolution covering the last 20 ka. Thus, the onset of the AHP is less well described than its termination. On the Pleistocene time scale, humid periods are characterized by high sedimentation rates and a large proportion of smectite and Fe-rich silicate minerals within the Nile delta sediment (Caley et al., 2011; Emeis et al., 2000; Kroon et al., 1998; Revel et al., 2010; Zhao et al., 2011). These characteristics reflect increased physical erosion and material transport mainly originating from the Ethiopian highland during higher rainfall regimes related to summer monsoon precessional variability. Thus, the sediment records preserved at the Nile deep-sea fan provide a suitable archive to study basin-wide environmental changes in vegetation cover, lithology, and soil erosion/weathering at a high time resolution mainly during humid periods such as the AHP (Blanchet et al., 2014; Castañeda et al., 2016; Hamann et al., 2009; Hennekam et al., 2015; Weldeab et al., 2014).

Sedimentary provenance of terrigenous material in the Nile deep-sea fan can be characterized through its neodymium isotopic signature (εNd, Bastian et al., 2017; Blanchet et al., 2014; Blanchet, 2019; Revel et al., 2015; Weldeab et al., 2002). No significant fractionation occurs during chemical weathering so εNd reflects the isotopic composition of the parent bedrock and the origin of the material (Bayon et al., 2015). Since the Nile basin encompasses the Precambrian African basement as well as the Ethiopian and Somalian Cenozoic basalts with contrasting Nd isotopic compositions, geochemical studies on its sediment loads can distinguish between the sources of the material (**Figure 1A**).

In parallel, glycerol dialkyl glycerol tetraethers (GDGTs), core membrane lipids of Achaea and Bacteria, are ubiquitous in marine to lacustrine waters and soils (e.g., Karner et al., 2001; Keough et al., 2003; Weijers et al., 2006). Specifically, the branched to isoprenoid tetraether ratio (BIT-index, Hopmans et al., 2004) and its first order derivatives are effective as tracers of continental inputs in estuarine settings (Blanchet et al., 2014; Kim et al., 2015; Ménot et al., 2006; Soulet et al., 2013). However, their environmental significance is

controversial (French et al., 2015; Kaiser et al., 2015; Zell et al., 2015). The BIT-index depends on the fluctuations of branched GDGTs (brGDGTs) and variation of the GDGT isoprenoid crenarchaeol (Hopmans et al., 2004). The index is therefore dependent on processes that affect these GDGTs. BIT values are not just dependent on the inputs of soil brGDGTs, but also on the levels of marine Archaea. For example, sites with equal inputs of terrestrial brGDGTs but different local marine productivity can display different BIT values (Fietz et al., 2011; Herfort et al., 2006; Smith et al., 2010). Furthermore, differential degradation in the water column may affect the relative preservation of different compounds. Field and laboratory experiments have tested the stability of brGDGTs from soils to river mouths (Peterse et al., 2015; Zhu et al., 2011). Exposure of anoxic sediments to oxygen produced little degradation of brGDGTs. This was likely due to their enhanced protection by the sedimentary matrix inhered in soils. However, this protection might differ for water-column produced isoprenoid GDGTs (Huguet et al., 2008; Kim et al., 2009). To avoid these possible biases, the abundance ratio of the hexa- to penta-methylated brGDGTs ratio (IIIa/IIa) was proposed (Xiao et al., 2016) and its modified form ΣIIIa/ΣIIa (Martin et al., 2019). In this study we used the ΣIIIa/ΣIIa ratio along with the proportions of tetra-, penta- and hexa-methylated brGDGTs, and the $\#rings_{tetra}$ index defined as the weighted mean number of pentacycles in tetramethylated brGDGTs (Sinninghe Damsté, 2016).

Using inorganic (Nd isotopes) and organic (GDGTs) proxies, we characterized the erosion products in the Nile delta to assess past hydrological changes in its basin. We validated the reliability of the targeted sedimentary archive by testing our toolbox on the termination of the AHP. We then discuss the timing and pattern of this wet period as recorded in the Nile delta in GDGT-based indices and clastic εNd signatures.

2. Hydrological/geological settings and materials

2.1 Present day hydrology and lithology of the Nile watershed

The Nile River system has a large drainage basin which extends over more than 30° in latitude from its sources to the delta (**Figure 1A**). During its journey through Eastern Africa, the river crosses hydroclimates ranging from subtropical at 15°N, with high precipitation (~1400 mm/year) to the Sahara Desert which receives ~5 mm/year (Korecha and Barnston, 2007). The precipitation regime along the Nile catchment is mainly related to the West African monsoon modulated by the Indian monsoon dynamic. It is characterized by intense rainfall during the June to September period in Ethiopia at ~15°N (250 mm/month (Korecha and Barnston, 2007)), and rainy seasons in April (~200 mm/month) and November (~150 mm/month) at 0–6°N latitude (Blanchet et al., 2015). Strengthening summer-season solar radiation and subsequent heating of the North African landmass creates a low-pressure zone that drives the inflow of moist air from the Atlantic and Indian tropical oceans to the landmass. During winter, winds are reversed, creating dry conditions across North Africa (Verschuren et al., 2009). Over Ethiopia, precipitation is fed by moisture originating from three sources: the Gulf of Guinea, the Indian Ocean and the northern region which consists of the Mediterranean Sea, Arabian Peninsula and the Red Sea (Viste and Sorteberg, 2013, light blue arrows on **Figure 1A**). A range of 69–95% and 5–24% of the total precipitation is derived from the Gulf of Guinea and Indian Ocean, respectively (Costa et al., 2014). Most of the wet months in Ethiopia occur in connection with enhanced moisture inflow through the northern branches (Viste and Sorteberg, 2013). Variations of the northern sources are less constrained but they are thought to be prone to greater deviations in the moisture contribution (Viste and Sorteberg, 2013).

Consistent with the latitudinal migration of the ITCZ through the year, two main sources of terrigenous material transported by the Nile River can be differentiated. One sediment source is located on the Ethiopian Traps and corresponds to the Blue/Atbara Nile

basin at 10–15°N. The other source is located on the Precambrian Craton and corresponds to the Equatorial basin at 0–10°N (Bahr el Jebel and White Nile branches) (**Figure 1A**). Due to its southern position, the Equatorial Nile provides a consistent flow of water during 8 months of the year because of the long wet season in the Equatorial Upland region (Nicholson, 2000). In contrast, the Blue Nile provides a relatively larger amount of water within a brief 3-month period when the African Rain Belt moves to the north during summer. Based on sampling along the Nile and detailed mineralogical and geochemical characterizations (including Nd isotopes), 96% of the particles deposited in the Nile deep sea fan today are estimated to originate from the Blue Nile and only 4% from the Equatorial Nile (Garzanti et al., 2015; Williams et al., 2015). Among the Blue Nile particles deposited, 91% originate from the Atbara Nile branch (Foucault and Stanley, 1989; Williams et al., 2015). The high degree of uplift in the East African Rift system, combined with heavy summer monsoonal rains in the Ethiopian Traps produces the highest erosion rates in the world (> 500 tons/ha/yr, Schüler et al., 2012; SCRP, 2000; Tebebu et al., 2010).

2.2 Late Pleistocene origin of terrestrial material on the Nile delta (Rosetta branch)

The western part of the Nile delta, the Rosetta branch, has been active since at least 115 ka BP and Nile River sediments have continuously and dominantly fed it (Ducassou et al., 2009; Mascle, 2014; Migeon et al., 2010; Revel et al., 2015). The highest sedimentation rates on the delta (up to ~400 cm/ka) have been recorded on the upper slope of the Rosetta levee (Ducassou et al., 2009, 2008) making this area a suitable candidate for high temporal resolution reconstructions using sedimentary proxies.

The lithology of the Ethiopian Traps includes Cenozoic basaltic Fe-rich silicate rocks related to the opening of the east African Rift system. These rocks are relatively more vulnerable to erosion in contrast to old craton metamorphic/granitic rocks of the Equatorial

Nile (Millot et al., 2002, **Figure 1A**). Thus, sedimentary εNd allows tracking of the temporal changes in the relative proportions of detrital sediment originating from the Ethiopian Traps (εNd > 0), the Equatorial craton (εNd ≈ –30), and the Saharan region (εNd ≈ –10 to –15) (**Figure 1A**, Revel et al., 2015; Weldeab et al., 2002). Examination of the finest (< 2 μm) clay-size detrital fraction of the sediments provides evidence for rapid transport of clays from the source to the deltaic sink without significant granulometric or mineralogical sorting occurring during sediment transport (Bastian et al., 2017). Nd and Li isotope data show that chemical weathering and subsequent physical erosion in the Nile basin rapidly responded to hydrological changes (Bastian et al., 2017). The highest clay-εNd values recorded during the AHP indicate larger proportions of clays derived from the Ethiopian Highland from 14 to ~8 ka BP. Thus, major remobilization and redeposition of original sediments primarily deposited on the continental shelf, upper slope or flood plain (Box et al., 2011) is likely negligible in the Nile system.

At the scale of the Holocene and the last deglaciation period, the substantial activity in the Rosetta system was confirmed by the range of sedimentation rates in sediment cores obtained on an east-west Nile delta transect (**Figure 1B–C**, Hennekam et al., 2015). Only cores taken on the western part of the Nile deltaic system show a large increase in sedimentation rate with laminated sediments during the AHP, in contrast to cores taken on its east side (**Figure 1B–C**).

2.3 Core site and chronology

The selected hemipelagic core (MS27PT – N31°47'90; E29°27'70; depth 1389 m; 7 m length) was taken less than ~90 km from the Nile Rosetta River mouth (**Figure 1B**). The age model of the core was constructed based on accelerator mass spectrometry ^{14}C dates. The age model has been published and refined by additional ^{14}C dates (**Table 1**, Revel et al., 2015,

2014, 2010). The top 315 cm of MS27PT covers the last 25.4 ka with laminated sediments from 10 to 7 cal ka BP and bioturbated sediments for the last deglacial period and the Late Holocene. The linear sedimentation rate (LSR) ranged from 2.8 cm/ka during LGM and 4 to 1.2 cal ka BP to 156 cm/ka during the early Holocene. LSR increased gradually from 6.5 to 120 cm/ka from 14 to 9.8 cal ka BP and a pulse at 3 cal ka BP was recorded (**Figure 1C,** Revel et al., 2015).

2.4 Elemental sediment analyses

Core MS27PT was analyzed using an Avaatech X-Ray Fluorescence (XRF) Core Scanner (Ifremer, Brest). Measurements were performed every 1 mm (cross core slit 10 mm and down core slit 1 mm) on the wet core surface, which was covered with a 4 μm SPEXCerti Ultralene foil before each analysis. We used a counting time of 20 s and tube energy settings of 10 kV during the analyses. Increase in sulfur intensity is likely related to authigenic pyrite formation under anoxic conditions. Taking a ratio to Cl reveals the presence of sulfur related to pyrites in excess of the constant S/Cl sea-salt ratio (Thomson et al., 2006). Hence, sulfur is presented in **Figure 2** normalized to chlorine. These results were confirmed by a few bulk mineralogy measurements, which indicate around 7% of pyrite at 8.9, 12, 12.2 cal ka BP and no pyrite at 12.5 cal ka BP (Bastian et al., personal com.).

Moreover, sulfur percentages were obtained from 18 discrete samples and were measured on a LEGO CS 300 carbon sulfur analyzer (LUSAC, Caen Normandie University) (Revel et al., 2010). Mn contents were measured by wavelength dispersive X-Ray Fluorescence (conventional destructive method) performed on 1 g of dry sediment material fused in glass discs (University of Claude-Bernard, Lyon). Accuracy and precision of Mn measurement were checked by international standard reference material and replicates of

analyses of selected samples. The analytical accuracy was within 1% of certified values and the precision was better than 3%.

2.5 Nd radiogenic isotopes

Chemical extractions of Nd isotopes in the core MS27PT (10 additional measurements to Revel et al., 2015 – in red in Table S1) were conducted at the Laboratory of Tectonophysics of Montpellier. Nd isotope ratios were measured on carbonate-free < 63 µm particle size using 100 mg of the dried alumino-silicate fraction. Each fraction corresponded to a 1 cm section cut along the sediment cores. Considering variations in sedimentation rates along sediment cores, this 1 cm cut corresponded to a time interval ranging from 10-70 years for humid periods and 400-1000 years for arid periods. Samples were leached for 1 hour with 1N HCl to dissolve biogenic carbonate. Leaching used the analytical sequential leaching procedure recommended by Bayon et al. (2002). The Fe-Mn oxyhydroxide fraction and organic carbon were removed using 10 ml 1M Hydroxylamine hydrochloride and 10 ml 5% H_2O_2, respectively. After leaching, the samples were centrifuged and the supernatant discarded. The remaining sediment was washed three times with ultra-pure water, discarding the supernatant each time, to remove the biogenic component and to eliminate any marine Nd isotope signal absorbed by the silt-clay fraction. The chemical separation of Nd included a first separation step using AG50W-X-8 cation exchange resin to collect rare earth elements followed by purification of Nd using HDEHP conditioned Teflon columns.

Nd isotopes were measured at the Ecole Normale Supérieure of Lyon (France) using a Thermo Scientific Neptune Plus MC-ICP-MS. The $^{143}Nd/^{144}Nd$ isotopic compositions were corrected from internal mass bias using an exponential law and a value of 0.7219 for the $^{146}Nd/^{144}Nd$ ratio. The external mass bias was corrected using standard bracketing method using AMES-Rennes analyzed each 2 unknowns. During the course of the study AMES-

Rennes (Chauvel and Blichert-Toft, 2001) standards yielded an average 0.512948±6 (2σ, n=10) for the $^{143}Nd/^{144}Nd$ ratio, respectively. Nd procedural blank measured during the course of this study was 25pg. Epsilon Nd values (εNd) were calculated using $^{143}Nd/^{144}Nd$ = 0.512638 (Bouvier et al., 2008).

2.6 GDGT extraction and analysis

Samples from core MS27PT were treated at LOCEAN (Sorbonne Universités) and also at CEREGE (**Table 2**). Additional sampling was conducted, from 207 to 303 cm depths, for every cm of the MS27PT core. All samples were analyzed in duplicate by high-performance liquid chromatography-mass spectrometry (HPLC/MS) at CEREGE following the protocols of Ménot and Bard (2012) and Sanchi et al. (2013). Semi-quantitative concentrations were calculated using a constant response factor between the C_{46} standard and GDGTs according to Huguet et al. (2006) and flux values were inferred.

In addition to these measurements, 60 samples from the MS27PT core (open symbols **Figure 2B–C**) were reanalyzed at CEREGE using a new chromatography method. The method used two ultra-high-performance liquid chromatography silica columns in series, which improved the separation of GDGTs (Davtian et al., 2018). This new method allowed the detection of new isomers and defining indices based on tetra-, penta- and hexa-methylated GDGT relative fractional abundances (Hopmans et al., 2016; Sinninghe Damsté, 2016).

2.7. GDGT-based proxies

The BIT index (Branched and Isoprenoid Tetraether index, range of values between 0 and 1) was proposed by Hopmans et al. (2004) as an indicator of terrigenous inputs. We calculated this index, as updated by Davtian et al. (2018), to account for the newest brGDGT isomers (De Jonge et al., 2013; Ding et al., 2016):

$$\mathrm{BIT} = \frac{\mathrm{Ia} + \mathrm{IIa_5} + \mathrm{IIIa_5} + \mathrm{IIa_6} + \mathrm{IIIa_6} + \mathrm{IIa_7} + \mathrm{IIIa_7}}{\mathrm{Crenarchaeol} + \mathrm{Ia} + \mathrm{IIa_5} + \mathrm{IIIa_5} + \mathrm{IIa_6} + \mathrm{IIIa_6} + \mathrm{IIa_7} + \mathrm{IIIa_7}}$$

Similarly the IIIa/IIa ratio proposed by Xiao et al., (2016) was calculated according to the following equation Martin et al. (2019):

$$\frac{\Sigma\mathrm{IIIa}}{\Sigma\mathrm{IIa}} = \frac{\mathrm{IIIa_5} + \mathrm{IIIa_6} + \mathrm{IIIa_7}}{\mathrm{IIa_5} + \mathrm{IIa_6} + \mathrm{IIa_7}}$$

Roman numerals refer to branched tetraether isomers following the nomenclature of Ding et al. (2016) (structures are shown in **Figure S1**). Crenarchaeol is the isoprenoid GDGT specific for Thaumarchaeota (Sinninghe Damsté et al., 2002).

The proportions of tetra- (I), penta- (II) and hexa- (III) -methylated brGDGTs were calculated using the fractional abundances of brGDGTs following Sinninghe Damsté (2016) including the 5 and 6-Me forms .

$$\%\mathrm{tetra} = \frac{\mathrm{Ia} + \mathrm{Ib} + \mathrm{Ic}}{\sum \mathrm{brGDGT}}$$

$$\%\mathrm{penta} = \frac{\sum_{\mathrm{i=5}}^{7} \mathrm{IIa_i} + \sum_{\mathrm{i=5}}^{6} \mathrm{IIb_i} + \sum_{\mathrm{i=5}}^{6} \mathrm{IIc_i}}{\sum \mathrm{brGDGT}}$$

$$\%\mathrm{hexa} = \frac{\sum_{\mathrm{i=5}}^{7} \mathrm{IIIa_i} + \sum_{\mathrm{i=5}}^{7} \mathrm{IIIb_i} + \sum_{\mathrm{i=5}}^{6} \mathrm{IIIc_i}}{\sum \mathrm{brGDGT}}$$

Finally, the weighted average number of cyclopentane moieties was calculated for tetramethylated brGDGTs as follows (Sinninghe Damsté, 2016):

$$\#rings_{tetra} = \frac{fI_b + 2 \times fI_c}{fI_a + fI_b + fI_c}$$

where fI_x stands for the fractional abundance of the tetra-methylated brGDGTs.

Mean analytical reproducibility of duplicated analyses of BIT-index and ΣIIIa/ΣIIa ratio were 0.007 and 0.002, respectively. BIT-index reproducibility is consistent with results from intercalibration activities conducted in 2009 and 2011. The Organic Geochemistry laboratory of CEREGE participated in these exercises (Schouten et al., 2013, 2009). BIT-

index and ΣIIIa/ΣIIa values derived from the new chromatography method exhibited a similar evolution through the entire core. For the ΣIIIa/ΣIIa index, lower values corresponded to larger shifts (without exceeding 0.1). For higher ΣIIIa/ΣIIa index values, differences were ~0.04. For the BIT-index, no systematic pattern was detected. Larger differences (0.09 unit) occurred between 220 and 280 cm without an obvious reason. The small shifts between the two data sets are well below the interlaboratory reproducibility experiment. These differences may have resulted from using distinct liquid chromatographic systems, atmospheric pressure chemical ionization conditions, chromatographic columns and solvent programs as well as the mass assignments for single ion monitoring analyses.

3. Results

3.1. εNd and sedimentation rate

The new εNd measurements (**Figure 2A**, red open circles) are consistent with previous εNd results (Revel et al., 2015). The εNd values varied from ~–4 during the African Humid Period (AHP) to –11 during Last Glacial Maximum (LGM) and late Holocene arid periods (**Figures 2A, Table S1**). From 14.5 ka BP and during the AHP, εNd values approached the Ethiopian Traps value (about 0). When combined with evidence of correspondingly high sedimentation rates (**Figure 2C, Table S1**), the more positive radiogenic εNd signature from 14.5 to 8.37 ka BP suggests enhanced delivery of detrital material from the Ethiopian Traps.

Increase in sulfur intensity (**Figure 2E**) in phase with the laminated sequence could be related to authigenic pyrite formation under anoxic conditions (Thomson et al., 2006) and/or could be related to dilution effect (e.g., decrease of another element). Few measurements of mineralogy indicate the formation of pyrite (7%) during the laminated sequence. Thus, the increase in S/Cl reveals the presence of additional S associated with

pyrite in excess of the constant S/Cl sea-salt ratio. The peak in Mn at 6 ka BP is more likely interpreted as a result of the reestablishment of oxic conditions (Thomson et al., 2006).

3.2. GDGT-based proxies

The BIT-index values ranged from 0.8 during the AHP (14, 12–8 ka BP) to 0.2 (at 8–7 ka BP) for core MS27PT (**Figure 2C**). The ΣIIIa/ΣIIa ratio varied between 0.2 and 0.9 with minimum values between 6.8 and 14.7 and abrupt positive excursions (> 0.6) at 20–15, 12.5, 3 ka BP (**Figure 2B**). Tetra- and penta-methylated fractional abundances ranged between 48–70% and 25–30%, respectively (**Figure 3B**). Hexa-methylated fractional abundances ranged between 4–12% (data not shown). Values of $\#rings_{tetra}$ were relatively constant along the core record and varied between 0.35 and 0.20 (data not shown).

Fluxes of brGDGTs and crenarchaeol showed similar patterns with values lower than 200 µg/cm^2/ka between the 20 to 15 ka BP interval and between 6.5 ka BP and the core top (**Figure 2D**). Maximum values of 2250 µg/cm^2/ka were measured between 14.5 and 6 ka BP. Despite the similar pattern, the crenarchaeol flux was relatively more abundant after 10 ka BP than before, when the opposite was true for brGDGTs.

The largest feature of the GDGT-based records are the substantial and synchronous changes that occur from ~12 to 7 ka BP in BIT, ΣIIIa/ΣIIa values as well as brGDGT and crenarchaeol abundances. These changes are concomitant with higher sedimentation rates and sulfur contents (**Figure 2C and E**). Moreover, a similar trend of variation was observed for εNd and ΣIIIa/ΣIIa values (**Figure 2A–B**).

4. Discussion

4.1. Evaluation of GDGTs as a proxy of soil and marine inputs

When compared to the available soil and marine sediment global database (Davtian et al., 2016; Xiao et al., 2016), the sedimentary ΣIIIa/ΣIIa values in core MS27PT clearly reflect a terrigenous signature (**Figure 3**). Most of the ΣIIIa/ΣIIa values ranged below the threshold of 0.59 as do 90% of the world soil values (Xiao et al., 2016). This is further confirmed by the proximity of most of the ΣIIIa/ΣIIa values in core MS27PT to the mean value of the few soils from the Nile watershed contained in the global soil database (0.14, **Figure 3**). ΣIIIa/ΣIIa values for periods outside the AHP fall within the deltaic interval as defined by Xiao et al., (2016). The ΣIIIa/ΣIIa ratio therefore seems to discriminate better than the BIT-index in the amount of river borne terrestrial supply.

Values of the $\#rings_{tetra}$ index lower than 0.7 confirmed the terrigenous origin of the tetraethers (Sinninghe Damsté, 2016). Similarly, penta- and tetra-methyl brGDGTs values in the Nile delta sediment core clustered close to the line of the soil global dataset (**Figure 3B**). Only a few data points were scattered towards lower abundances of tetramethyl brGDGTs. These corresponded to sediments older than the AHP that exhibited higher ΣIIIa/ΣIIa ratios (**Figure 3A**).

The effect of temperature on brGDGTs largely reported in literature (e.g. (Peterse et al., 2012; Tierney et al., 2010; Weijers et al., 2007)) seems to be partially overprinted by the changes in their sources, but it might explain part of the scatter described in the previous paragraphs. Data-points with higher ΣIIIa/ΣIIa values indeed correspond to lower tetramethyl brGDGT percentages (**Figure 3B**) and therefore low temperatures (Martin et al., 2019; Tierney et al., 2010; Weijers et al., 2007). As such, some of the higher ΣIIIa/ΣIIa values during the time interval from 14.7 to 22 ka may be affected by temperature. Still, the similar variability in the independent proxy εNd, points to a terrigenous origin of the ΣIIIa/ΣIIa signal. The ΣIIIa/ΣIIa variability in the rest of the Holocene cannot be explained by temperature and, hence, must be due to changes in terrigenous input.

4.2. Reinterpretation of the BIT-index in estuarine settings

The dominant feature of the BIT-index record is the high values (> 0.4) before and during the AHP (~15 to 8.5 ka BP). The concomitance of these maxima with high sedimentation rates and less radiogenic εNd values supports its interpretation as a terrigenous input and a tropical Ethiopian soil erosion marker. They are also associated with higher concentrations of brGDGTs (**Figure 2**). For the end of the AHP, these results are consistent, both in timing and amplitude, with those of Blanchet et al. (2014) based on the same proxy. This confirms the local representativeness of our signal (**Figure 4B–C**).

The initial interpretation of the BIT-index as a proxy of terrigenous supply is, however, challenged when different proxies are cross-compared, especially for the end of the AHP. From 12 to 6 ka, high insolation is associated with large terrigenous supply as indicated by high sedimentation rates, biomarker fluxes and BIT-index values as well as low ΣIIIa/ΣIIa values (**Figure 2B-D**). Between 8.5 and 6 ka BP, however, BIT-index decreases consistently with relatively high fluxes of crenarchaeol relative to brGDGT values and as well as a maximum in sulfur concentrations (**Figure 2D–E**). Large concentrations of crenarchaeol could have resulted from either enhanced marine surface productivity and/or enhanced deep-sea floor preservation. A high sulfur content in sediments indicates anoxic conditions at the sea floor and related formation of sulfide minerals (Passier et al., 1999). These conditions probably led to enhanced crenarchaeol preservation and decreased BIT-index values (Huguet et al., 2008). Bottom water anoxia is indicated by the laminations of the sediment deposits during this time period (**Figure 2**, Ducassou et al., 2008) and the presence of pyrite (see the methodology). An abrupt peak of Mn at ~6 ka BP reflects deep water re-oxygenation when the eastern Mediterranean overturning circulation resumed (**Figure 2E,** De Lange et al., 2008; Tachikawa et al., 2015; Thomson et al., 2006). The presence of a

unique Mn peak, instead of an extra "older" Mn peak, only at the end of the anoxic event, suggests that post deposition oxidation was largely absent. This was likely due to the high sediment accumulation rates, circumventing post-depositional diagenesis (De Lange et al., 2008). Associated with the resumption of the eastern Mediterranean overturning circulation, water column oxidation caused enhanced degradation of crenarchaeol compared to brGDGTs and possibly an "artificial" increase of BIT-index values (Huguet et al., 2008; Peterse et al., 2015). The absence of a return to pre-AHP values for the BIT-index, in contrast to IIIa/IIa, may be attributed to the modern sea-level high-stand leading to relatively higher crenarchaeol production in the water column (**Figure 4A**).

The difference, both in amplitude of the GDGT signals of the cores collected close to the Nile mouth (this study and Blanchet et al., 2014) and on the Israeli coast (Castaneda et al., 2010), probably reflects different origins or different distances to the source material (**Figure 4**). The surface productivity changes, represented by crenarchaeol concentrations, seem to be controlled on the basin scale and are homogeneous in the western and eastern provinces. Similarly, the first-order variations in terrigenous fluxes, as recorded by sedimentation rates, significantly differ (**Figure 1C**) and challenge the interpretation that BIT-index variations are associated with differential responses of soil erosion (Kim et al., 2015, 2014). The lag between erosion and terrigenous supply reported by previous studies in the Eastern Mediterranean Sea (Blanchet et al., 2014; Castañeda et al., 2016) could therefore be due to a misinterpretation of the BIT-index.

The co-evolution of the εNd and ΣIIIa/ΣIIa patterns is most likely due to increased terrigenous inputs, from 14.5 to ~7 ka BP, essentially reflecting enhanced physical erosion and transport processes from the Ethiopian Traps exposed to a high precipitation regime. For this reason, we favor the ΣIIIa/ΣIIa ratio as a tracer of the terrigenous input from the Nile River.

4.3. Stepwise onset of the African Humid Period

Downcore εNd, ΣIIIa/ΣIIa ratio and sedimentation rates in the Rosetta Nile delta follow the overall trend of the 15°N summer insolation intensity. Nile sediment cores record apparently stable humid conditions from 14.5 to 8.4 ka BP confirming the occurrence of strong monsoons and intense precipitation regimes in the regional tropical Ethiopian Highland (**Figure 5**). The direct response of physical erosion and silicate weathering to increased precipitation is understood based on Nd isotope levels in the clay fraction (Bastian et al., 2017). The synchronous shift of GDGT-based proxies from a marine to a soil dominated origin indicates a rapid increase of soil erosion and confirms the high transport efficiency of suspended matter within the Nile River basin.

The control of insolation on precipitation regimes is well established during the AHP (deMenocal et al., 2000; Gasse, 2000; Shanahan et al., 2015) and the centennial-resolution of our record shows a gradual transition from the LGM arid to humid conditions over the Nile watershed within about 2 ka. The ΣIIIa/ΣIIa and εNd signals deviate as early as 14.8 ka BP (immediately after the Heinrich stadial 1) and full humid conditions were reached at 12 ka BP after the end of the Younger Dryas (YD). The early onset of the AHP exhibited by both organic and inorganic proxies is consistent with other precipitation records around Africa independent of the latitude studied (**Figure 5**). These proxies include leaf waxes, isotopic records (Costa et al., 2014; Shanahan et al., 2015; Tierney et al., 2008) and reconstructed lake levels (Armitage et al., 2015). The main discrepancy among the previous studies is the pattern of variation. The precipitation amount increased faster in the northern than in the southern latitudes. Furthermore, the East African records show a stepwise evolution that might be attributed to a different moisture source through the migration of the Congo Air Boundary (CAB, **Figure 1A**). Both rapid increases are attributed to CO_2-driven deglacial tropical sea

surface temperature (SST) increase and atmospheric warming. This led to increasing atmospheric moisture, resumption of the Atlantic Meridional Overturning Circulation (AMOC) and to an increase in the northern high-latitude SST. All of these factors allowed the rain belt to penetrate further north (Collins et al., 2017).

4.4. Early stepwise termination of the African Humid Period

The beginning of the modern hydrology of the Nile at the end of AHP has been controversial. Timing issues have been studied using lacustrine and marine sedimentary records and modeling experiments (Blanchet et al., 2014; Castañeda et al., 2016; Claussen et al., 2013; Lezine et al., 2011; Tierney and deMenocal, 2013). Nile delta sedimentary records exhibit a progressive decrease, both in εNd and GDGT-based proxies, which was initiated as early as 8.5 ka (**Figure 5A**). This indicates a gradually decreasing influence of erosion materials from the Ethiopian Traps associated with the southern migration of the rain belt. This is consistent with studies using $^{87}Sr/^{86}Sr$ records (Cole et al., 2009; Jung et al., 2004) and results of geochemistry and Li and Nd isotopes measured in the clay fraction (Bastian et al., 2017; Liu et al., 2017). However, the evolution of inorganic and organic proxies is consistently indicating a synchronous response of the bedrock and soil erosion to precipitation changes, which may be contrary to previous studies (Blanchet et al., 2014; Castañeda et al., 2016), but is in agreement with the initiation of the AHP This is further supported by the ΣIIIa/ΣIIa ratio and it is consistent with the progressive decline in the Ba/Ca ratio (core SL112, Weldeab et al., 2014) that commenced at 7.8 ka BP.

The large catchment area of the Nile allows evaluation, through high-resolution deep-sea fan sediment records, of the transient onset and termination of the AHP following the evolution of summer insolation. The latitudinal migration of the ITCZ is the primary factor controlling the precipitation on the Ethiopian highlands, while the west/east contrast in

precipitation response might be linked to the Congo Air boundary (Costa et al., 2014). Our synthesis (**Figure 5**) indicates that a first manifestation of less humid conditions began almost everywhere around 8.4 ka BP in Africa. At Lake Tanganyika this was expressed as a short punctual event. In other records, it clearly appears as a step-by-step decrease until 6.5 ka BP. Insolation orbital forcing was primarily responsible for the beginning of arid conditions around 4 ka BP in phase with the maximum of precession and minimum of summer insolation (**Figure 5A**). We propose that between 8.5 and 6.5 ka BP, the changes in both ΣIIIa/ΣIIa ratio and εNd value represent the beginning of the end of the AHP, occurring within 4 ka (**Figure 4**). This gradual decrease could also be directly linked to the decrease of insolation.

4.5. Strong imprint of the Younger Dryas event

Organic and inorganic records from the Nile delta both exhibit a pronounced shift towards a decrease in Blue Nile flood discharges, suggesting less precipitation in the Ethiopian Highlands during the Younger Dryas (**Figure 4-5**). A different picture emerges from hydrological records over Africa (Garcin et al., 2007; Gasse, 2000) with northern lake records indicating a step-wise reduction of precipitation (Costa et al., 2014; Marshall et al., 2011). The shift towards dryer conditions during the Younger Dryas is well documented in the central and west African records and for latitudes higher than 8°N (**Figure 5**). This indicates a more southward shift of the Intertropical convergence zone (ITCZ) driven by Northern Hemisphere hydrological changes as well as the influence of distinct moisture sources contributing to the precipitation.

Conclusions

A comparison of organic and inorganic signatures in a sedimentary sequence from the Nile deep-sea fan over the last 20 ka as well as a centennial time resolution for key intervals such as the onset and termination of the AHP produced the following conclusions:

1. The reliability, with qualifications, of the use of brGDGTs as a terrigenous flux tracer in a deltaic environment,

2. The diversity of sedimentary settings in the Nile delta based on a synthesis of local scale publications,

3. The fluctuations of terrigenous inputs as retraced by εNd and brGDGTs records driven by summer insolation,

4. The stepwise onset of the AHP at 14.8 ka as well as the early initiation of the AHP termination at 8.5 ka. The stepwise termination pattern to a modern hydrology state occurred within 4 ka,

5. The imprint of abrupt "North Atlantic events" such as the Younger Dryas in the Nile sedimentary sequence. To a lesser extent, the 8.2 ka event was a tipping point in the low latitude paleorecord.

Our conclusions indicate the need for additional high temporal resolution studies involving coupling of independent tracers and modelling experiments. This information will better explain the drivers of the abrupt changes recorded in sediments at low latitudes as well as the propagation of these changes to the Mediterranean Sea area. Also, the effects of Nile freshwater releases in the Mediterranean Sea on the North Atlantic climate need to be studied (Swingedouw et al., 2019).

Acknowledgements

CEREGE research was supported by the Collège de France and studies focusing on low latitudes were supported by the BNP Paribas Foundation (Climate Initiative – project CPATEMP). Internship gratification for SP was financed through a project LABEX OT-Med (Objectif Terre: Bassin Méditerranéen; http://www.otmed.fr/; Project "MEDiterranean surface HYydrology during abrupt climatic events" – MEDHY, P.I. GM). GDGTs and εNd costs were partially covered by the program MADHO (INSU MISTRALS – P.I. MR) and by a BQR (Geoazur – P.I. MR).

References

Armitage, S.J., Bristow, C.S., Drake, N.A., 2015. West African monsoon dynamics inferred from abrupt fluctuations of Lake Mega-Chad. Proceedings of the National Academy of Sciences 112, 8543–8548. https://doi.org/10.1073/pnas.1417655112

Bastian, L., Revel, M., Bayon, G., Dufour, A., Vigier, N., 2017. Abrupt response of chemical weathering to Late Quaternary hydroclimate changes in northeast Africa. Scientific Reports 7, 44231.

Bayon, G., German, C.R., Boella, R.M., Milton, J.A., Taylor, R.N., Nesbitt, R.W., 2002. An improved method for extracting marine sediment fractions and its application to Sr and Nd isotopic analysis. Chemical Geology 187, 179–199. https://doi.org/10.1016/S0009-2541(01)00416-8

Bayon, G., Toucanne, S., Skonieczny, C., André, L., Bermell, S., Cheron, S., Dennielou, B., Etoubleau, J., Freslon, N., Gauchery, T., Germain, Y., Jorry, S.J., Ménot, G., Monin, L., Ponzevera, E., Rouget, M.-L., Tachikawa, K., Barrat, J.A., 2015. Rare earth elements and neodymium isotopes in world river sediments revisited. Geochimica et Cosmochimica Acta 170, 17–38. https://doi.org/10.1016/j.gca.2015.08.001

Berger, A., 1981. The astronomical theory of paleoclimates A. Berger, in: Climatic Variations and Variability: Facts and Theories. Dordrecht Holland, pp. 501–525.

Berke, M.A., Johnson, T.C., Werne, J.P., Schouten, S., Sinninghe Damsté, J.S., 2012. A mid-Holocene thermal maximum at the end of the African Humid Period. Earth and Planetary Science Letters 351–352, 95–104. https://doi.org/10.1016/j.epsl.2012.07.008

Blanchet, C., Tjallingii, R., Frank, M., Lorenzen, J., Reitz, A., Brown, K., Feseker, T., Brückmann, W., 2013. High- and low-latitude forcing of the Nile River regime during the Holocene inferred from laminated sediments of the Nile deep-sea fan. Earth and Planetary Science Letters 364, 98–110. https://doi.org/10.1016/j.epsl.2013.01.009

Blanchet, C.L., 2019. A database of marine and terrestrial radiogenic Nd and Sr isotopes for tracing earth-surface processes. Earth System Science Data 11, 741–759. https://doi.org/10.5194/essd-11-741-2019

Blanchet, Contoux, C., Leduc, G., 2015. Runoff and precipitation dynamics in the Blue and White Nile catchments during the mid-Holocene: A data-model comparison. Quaternary Science Reviews 130, 222–230. https://doi.org/10.1016/j.quascirev.2015.07.014

Blanchet, Frank, M., Schouten, S., 2014. Asynchronous Changes in Vegetation, Runoff and Erosion in the Nile River Watershed during the Holocene. PLOS ONE 9, e115958. https://doi.org/10.1371/journal.pone.0115958

Bouvier, A., Vervoort, J.D., Patchett, P.J., 2008. The Lu–Hf and Sm–Nd isotopic composition of CHUR: Constraints from unequilibrated chondrites and implications for the bulk composition of terrestrial planets. Earth and Planetary Science Letters 273, 48–57. https://doi.org/10.1016/j.epsl.2008.06.010

Box, M.R., Krom, M.D., Cliff, R.A., Bar-Matthews, M., Almogi-Labin, A., Ayalon, A., Paterne, M., 2011. Response of the Nile and its catchment to millennial-scale climatic change since the LGM from Sr isotopes and major elements of East Mediterranean sediments. Quaternary Science Reviews 30, 431–442. https://doi.org/10.1016/j.quascirev.2010.12.005

Caley, T., Malaizé, B., Revel, M., Ducassou, E., Wainer, K., Ibrahim, M., Shoeaib, D., Migeon, S., Marieu, V., 2011. Orbital timing of the Indian, East Asian and African boreal monsoons and the concept of a 'global monsoon.' Quaternary Science Reviews 30, 3705–3715. https://doi.org/10.1016/j.quascirev.2011.09.015

Castaneda, I.S., Schefu[ss], E., Pätzold, J., Sinninghe Damste, J.S., Weldeab, S., Schouten, S., 2010. Millenial-scale sea surface temperature changes in the Eastern Mediterranean (Nile River Delta Region) over the last 27,000 years. Paleoceanography 25, PA1208. https://doi.org/10.1029/2009PA001740

Castañeda, I.S., Schouten, S., Pätzold, J., Lucassen, F., Kasemann, S., Kuhlmann, H., Schefuß, E., 2016. Hydroclimate variability in the Nile River Basin during the past 28,000 years. Earth and Planetary Science Letters 438, 47–56. https://doi.org/10.1016/j.epsl.2015.12.014

Chauvel, C., Blichert-Toft, J., 2001. A hafnium isotope and trace element perspective on melting of the depleted mantle. Earth and Planetary Science Letters 190, 137–151. https://doi.org/10.1016/S0012-821X(01)00379-X

Claussen, M., Bathiany, S., Brovkin, V., Kleinen, T., 2013. Simulated climate-vegetation interaction in semi-arid regions affected by plant diversity. Nature Geosci 6, 954–958.

Cole, J.M., Goldstein, S.L., deMenocal, P.B., Hemming, S.R., Grousset, F.E., 2009. Contrasting compositions of Saharan dust in the eastern Atlantic Ocean during the last deglaciation and African Humid Period. Earth and Planetary Science Letters 278, 257–266. https://doi.org/10.1016/j.epsl.2008.12.011

Collins, J.A., Prange, M., Caley, T., Gimeno, L., Beckmann, B., Mulitza, S., Skonieczny, C., Roche, D., Schefuß, E., 2017. Rapid termination of the African Humid Period triggered by northern high-latitude cooling. Nature Communications 8, 1372. https://doi.org/10.1038/s41467-017-01454-y

Costa, K., Russell, J., Konecky, B., Lamb, H., 2014. Isotopic reconstruction of the African Humid Period and Congo Air Boundary migration at Lake Tana, Ethiopia. Quaternary Science Reviews 83, 58–67. https://doi.org/10.1016/j.quascirev.2013.10.031

Davtian, N., Bard, E., Ménot, G., Fagault, Y., 2018. The importance of mass accuracy in selected ion monitoring analysis of branched and isoprenoid tetraethers. Organic Geochemistry 118, 58–62. https://doi.org/10.1016/j.orggeochem.2018.01.007

Davtian, N., Ménot, G., Bard, E., Poulenard, J., Podwojewski, P., 2016. Consideration of soil types for the calibration of molecular proxies for soil pH and temperature using global soil datasets and Vietnamese soil profiles. Organic Geochemistry 101, 140–153. https://doi.org/10.1016/j.orggeochem.2016.09.002

De Jonge, C., Hopmans, E.C., Stadnitskaia, A., Rijpstra, W.I.C., Hofland, R., Tegelaar, E., Sinninghe Damsté, J.S., 2013. Identification of novel penta- and hexamethylated branched glycerol dialkyl glycerol tetraethers in peat using HPLC–MS2, GC–MS and GC–SMB-MS. Organic Geochemistry 54, 78–82. https://doi.org/10.1016/j.orggeochem.2012.10.004

De Jonge, C., Stadnitskaia, A., Cherkashov, G., Sinninghe Damsté, J.S., 2016. Branched glycerol dialkyl glycerol tetraethers and crenarchaeol record post-glacial sea level rise and shift in source of terrigenous brGDGTs in the Kara Sea (Arctic Ocean). Organic Geochemistry 92, 42–54. https://doi.org/10.1016/j.orggeochem.2015.11.009

De Jonge, C., Stadnitskaia, A., Hopmans, E.C., Cherkashov, G., Fedotov, A., Streletskaya, I.D., Vasiliev, A.A., Sinninghe Damsté, J.S., 2015. Drastic changes in the distribution of branched tetraether lipids in suspended matter and sediments from the Yenisei River and Kara Sea (Siberia): Implications for the use of brGDGT-based proxies in coastal marine sediments. Geochimica et Cosmochimica Acta 165, 200–225. https://doi.org/10.1016/j.gca.2015.05.044

De Lange, G.J., Thomson, J., Reitz, A., Slomp, C.P., Speranza Principato, M., Erba, E., Corselli, C., 2008. Synchronous basin-wide formation and redox-controlled preservation of a Mediterranean sapropel. Nature Geosci 1, 606–610. https://doi.org/10.1038/ngeo283

deMenocal, P., Ortiz, J., Guilderson, T., Sarnthein, M., 2000. Coherent High- and Low-Latitude Climate Variability During the Holocene Warm Period. Science 288, 2198–2202.

Ding, S., Schwab, V.F., Ueberschaar, N., Roth, V.-N., Lange, M., Xu, Y., Gleixner, G., Pohnert, G., 2016. Identification of novel 7-methyl and cyclopentanyl branched glycerol dialkyl glycerol tetraethers in lake sediments. Organic Geochemistry 102, 52–58. https://doi.org/10.1016/j.orggeochem.2016.09.009

Ducassou, E., Migeon, S., Mulder, Thierry, Murat, Anne, Capotondi, Lucilla, Bernasconi, Stephano, M., Mascle, Jean, 2009. Evolution of the Nile deep-sea turbidite system during the Late Quaternary: influence of climate change on fan sedimentation. Sedimentology 56, 2061–2090.

Ducassou, E., Mulder, T., Migeon, S., Gonthier, E., Murat, A., Revel, M., Capotondi, L., Bernasconi, S.M., Mascle, J., Zaragosi, S., 2008. Nile floods recorded in deep Mediterranean sediments. Quaternary Research 70, 382–391. https://doi.org/10.1016/j.yqres.2008.02.011

Emeis, K.-C., Struck, U., Schulz, H.-M., Rosenberg, R., Bernasconi, S., Erlenkeuser, H., Sakamoto, T., Martinez-Ruiz, F., 2000. Temperature and salinity variations of Mediterranean Sea surface waters over the last 16,000 years from records of planktonic stable oxygen isotopes and alkenone unsaturation ratios. Palaeogeography, Palaeoclimatology, Palaeoecology 158, 259–280.

Fietz, S., Martínez-Garcia, A., Huguet, C., Rueda, G., Rosell-Melé, A., 2011. Constraints in the application of the Branched and Isoprenoid Tetraether index as a terrestrial input proxy. J. Geophys. Res. 116, n/a-n/a. https://doi.org/10.1029/2011JC007062

Foerster, V., Junginger, A., Langkamp, O., Gebru, T., Asrat, A., Umer, M., Lamb, H.F., Wennrich, V., Rethemeyer, J., Nowaczyk, N., Trauth, M.H., Schaebitz, F., 2012. Climatic change recorded in the sediments of the Chew Bahir basin, southern Ethiopia, during the last 45,000 years. Quaternary International 274, 25–37. https://doi.org/10.1016/j.quaint.2012.06.028

Foucault, A., Stanley, D.J., 1989. Late Quaternary palaeoclimatic oscillations in East Africa recorded by heavy minerals in the Nile delta. Nature 339, 44–46. https://doi.org/10.1038/339044a0

French, D.W., Huguet, C., Turich, C., Wakeham, S.G., Carlson, L.T., Ingalls, A.E., 2015. Spatial distributions of core and intact glycerol dialkyl glycerol tetraethers (GDGTs) in the Columbia River Basin and Willapa Bay, Washington: Insights into origin and implications for the BIT index. Organic Geochemistry 88, 91–112. https://doi.org/10.1016/j.orggeochem.2015.09.001

Garcin, Y., Deschamps, P., Ménot, G., de Sauliey, G., Schefu[ss], E., Sebag, D., Dupont, L.M., Oslisly, R., Brademan, B., Mbusnum, K., Onana, J.-M., Ako, A.A., Epp, L.S., Tjallingii, R., Strecker, M.R., Brauer, A., Sachse, D., 2018. Early anthropogenic impact on Western Central African rainforests 2,600 years ago. PNAS. https://doi.org/10.1073/pnas.1715336115

Garzanti, E., Andò, S., Padoan, M., Vezzoli, G., El Kammar, A., 2015. The modern Nile sediment system: Processes and products. Quaternary Science Reviews 130, 9–56. https://doi.org/10.1016/j.quascirev.2015.07.011

Gasse, F., 2000. Hydrological changes in the African tropics since the Last Glacial Maximum. Quaternary Science Reviews 19, 189–211. https://doi.org/10.1016/S0277-3791(99)00061-X

Goiran, J.-P., 2001. Recherches géomorphologiques dans la région littorale d'Alexandrie en Egypte (Sciences de l'Homme et Société). Université de Provence - Aix-Marseille I.

Grousset, F.E., Biscaye, P.E., 2005. Tracing dust sources and transport patterns using Sr, Nd and Pb isotopes. Chemical Geology 222, 149–167. https://doi.org/10.1016/j.chemgeo.2005.05.006

Hamann, Y., Ehrmann, W., Schmiedl, G., Kuhnt, T., 2009. Modern and late Quaternary clay mineral distribution in the area of the SE Mediterranean Sea. Quaternary Research 71, 453–464. https://doi.org/10.1016/j.yqres.2009.01.001

Hennekam, R., Donders, T.H., Zwiep, K., de Lange, G.J., 2015. Integral view of Holocene precipitation and vegetation changes in the Nile catchment area as inferred from its delta sediments. Quaternary Science Reviews 130, 189–199. https://doi.org/10.1016/j.quascirev.2015.05.031

Hennekam, R., Jilbert, T., Schnetger, B., de Lange, G.J., 2014. Solar forcing of Nile discharge and sapropel S1 formation in the early to middle Holocene eastern Mediterranean. Paleoceanography 29, 343–356. https://doi.org/10.1002/2013PA002553

Herfort, L., Schouten, S., Boon, J.P., Woltering, M., Baas, M., Weijers, J.W.H., Sinninghe Damsté, J.S., 2006. Characterization of transport and deposition of terrestrial organic matter in the southern North Sea using the BIT index. Limnol. Oceanogr. 51, 2196–2205. https://doi.org/10.4319/lo.2006.51.5.2196

Hopmans, E.C., Schouten, S., Sinninghe Damsté, J.S., 2016. The effect of improved chromatography on GDGT-based palaeoproxies. Organic Geochemistry 93, 1–6. https://doi.org/10.1016/j.orggeochem.2015.12.006

Hopmans, E.C., Weijers, J.W.H., Schefu[ss], E., Herfort, L., Sinninghe Damste, J.S., Schouten, S., 2004. A novel proxy for terrestrial organic matter in sediments based on branched and isoprenoid tetraether lipids. Earth and Planetary Science Letters 224, 107–116.

Huguet, C., de Lange, G.J., Gustafsson, Ö., Middelburg, J.J., Sinninghe Damsté, J.S., Schouten, S., 2008. Selective preservation of soil organic matter in oxidized marine sediments (Madeira Abyssal Plain). Geochimica et Cosmochimica Acta 72, 6061–6068. https://doi.org/10.1016/j.gca.2008.09.021

Huguet, C., Hopmans, E.C., Febo-Ayala, W., Thompson, D.H., Sinninghe Damsté, J.S., Schouten, S., 2006. An improved method to determine the absolute abundance of glycerol dibiphytanyl glycerol tetraether lipids. Organic Geochemistry 37, 1036–1041.

Jung, S.J.A., Davies, G.R., Ganssen, G.M., Kroon, D., 2004. Stepwise Holocene aridification in NE Africa deduced from dust-borne radiogenic isotope records. Earth and Planetary Science Letters 221, 27–37. https://doi.org/10.1016/S0012-821X(04)00095-0

Kaiser, J., Schouten, S., Kilian, R., Arz, H.W., Lamy, F., Sinninghe Damsté, J.S., 2015.

Isoprenoid and branched GDGT-based proxies for surface sediments from marine, fjord and lake environments in Chile. Organic Geochemistry 89–90, 117–127. https://doi.org/10.1016/j.orggeochem.2015.10.007

Karner, M.B., DeLong, E.F., Karl, D.M., 2001. Archaeal dominance in the mesopelagic zone of the Pacific Ocean. Nature 409, 507–510.

Keough, B.P., Schmidt, T.M., Hicks, R.E., 2003. Archaeal Nucleic Acids in Picoplankton from Great Lakes on Three Continents. Microb Ecol 46, 238–248.

Kim, J.-H., Buscail, R., Fanget, A.-S., Eyrolle-Boyer, F., Bassetti, M.-A., Dorhout, D., Baas, M., Berné, S., Sinninghe Damsté, J.S., 2014. Impact of river channel shifts on tetraether lipids in the Rhône prodelta (NW Mediterranean): Implication for the BIT index as an indicator of palaeoflood events. Organic Geochemistry 75, 99–108. https://doi.org/10.1016/j.orggeochem.2014.06.011

Kim, J.-H., Huguet, C., Zonneveld, K.A.F., Versteegh, G.J.M., Roeder, W., Sinninghe Damsté, J.S., Schouten, S., 2009. An experimental field study to test the stability of lipids used for the TEX86 and palaeothermometers. Geochimica et Cosmochimica Acta 73, 2888–2898. https://doi.org/doi: 10.1016/j.gca.2009.02.030

Kim, J.-H., Ludwig, W., Buscail, R., Dorhout, D., Sinninghe Damsté, 2015. Tracing tetraether lipids from source to sink in the Rhône River system (NW Mediterranean). Front. Earth Sci.

Korecha, D., Barnston, A.G., 2007. Predictability of June–September Rainfall in Ethiopia. Mon. Wea. Rev. 135, 628–650. https://doi.org/10.1175/MWR3304.1

Kroon, D., Alexander, I., Little, M., Lourens, L.J., Matthewson, A., Robertson, A.H.F., Sakamoto, T., 1998. Oxygen isotope and Sapropel stratigraphy in the eastern Mediterranean during the last 3.2 million years. Proceedings of the Ocean Drilling Program: Scientific Results 160, 181–190.

Kropelin, S., Verschuren, D., Lezine, A.M., Eggermont, H., Cocquyt, C., Francus, P., Cazet, J.P., Fagot, M., Rumes, B., Russell, J.M., Darius, F., Conley, D.J., Schuster, M., von Suchodoletz, H., Engstrom, D.R., 2008. Climate-driven ecosystem succession in the Sahara: The past 6000 years. Science 320, 765–768. https://doi.org/10.1126/science.1154913|ISSN

Kuper, R., Kropelin, S., 2006. Climate-controlled Holocene occupation in the Sahara: Motor of Africa's evolution. Science 313, 803–807. https://doi.org/10.1126/science.1130989|ISSN

Lezine, A.M., Hely, C., Grenier, C., Braconnot, P., Krinner, G., 2011. Sahara and Sahel vulnerability to climate changes, lessons from Holocene hydrological data. Quaternary Science Reviews 30, 3001–3012. https://doi.org/10.1016/j.quascirev.2011.07.006

Liu, X., Rendle-Bühring, R., Kuhlmann, H., Li, A., 2017. Two phases of the Holocene East African Humid Period: Inferred from a high-resolution geochemical record off Tanzania. Earth and Planetary Science Letters 460, 123–134. https://doi.org/10.1016/j.epsl.2016.12.016

Loomis, S.E., Russell, J.M., Lamb, H.F., 2015. Northeast African temperature variability since the Late Pleistocene. Palaeogeography, Palaeoclimatology, Palaeoecology 423, 80–90. https://doi.org/10.1016/j.palaeo.2015.02.005

Martin, C., Ménot, G., Thouveny, N., Davtian, N., Andrieu-Ponel, V., Reille, M., Bard, E., 2019. Impact of human activities and vegetation changes on the tetraether sources in Lake St Front (Massif Central, France). Organic Geochemistry 135, 38–52. https://doi.org/10.1016/j.orggeochem.2019.06.005

Mascle, J., 2014. The Nile continental margin, a compendium compiled by Jean Mascle. Marine Geology 358, 1–510.

McGee, D., deMenocal, P.B., Winckler, G., Stuut, J.B.W., Bradtmiller, L.I., 2013. The magnitude, timing and abruptness of changes in North African dust deposition over the last 20,000 yr. Earth and Planetary Science Letters 371–372, 163–176. https://doi.org/10.1016/j.epsl.2013.03.054

Ménot, G., Bard, E., 2012. A precise search for drastic temperature shifts of the past 40,000 years in southeastern Europe. Paleoceanography 27, PA2210. https://doi.org/10.1029/2012PA002291

Ménot, G., Bard, E., Rostek, F., Weijers, J., Hopmans, E.C., Schouten, S., Sinninghe Damsté, J.S., 2006. Early reactivation of european rivers during the last deglaciation. Science 313, 1623–1625.

Migeon, S., Ducassou, E., Le Gonidec, Y., Rouillard, P., Mascle, J., Revel-Rolland, M., 2010.

Lobe construction and sand/mud segregation by turbidity currents and debris flows on the western Nile deep-sea fan (Eastern Mediterranean). Sedimentary Geology 229, 124–143. https://doi.org/10.1016/j.sedgeo.2010.02.011

Millot, R., Gaillardet, J., Dupré, B., Allègre, C.J., 2002. The global control of silicate weathering rates and the coupling with physical erosion: new insights from rivers of the Canadian Shield. Earth and Planetary Science Letters 196, 83–98. https://doi.org/10.1016/S0012-821X(01)00599-4

Naafs, B.D.A., Gallego-Sala, A.V., Inglis, G.N., Pancost, R.D., 2017. Refining the global branched glycerol dialkyl glycerol tetraether (brGDGT) soil temperature calibration. Organic Geochemistry 106, 48–56. https://doi.org/10.1016/j.orggeochem.2017.01.009

Nicholson, S.E., 2000. The nature of rainfall variability over Africa on time scales of decades to millenia. Global and Planetary Change 26, 137–158. https://doi.org/10.1016/S0921-8181(00)00040-0

Passier, H.F., Bosch, H.-J., Nijenhuis, I.A., Lourens, L.J., Bottcher, M.E., Leenders, A., Damste, J.S.S., de Lange, G.J., Leeuw, J.W., 1999. Sulphidic Mediterranean surface waters during Pliocene sapropel formation. Nature 397, 146–149. https://doi.org/10.1038/16441

Peterse, F., Moy, C.M., Eglinton, T.I., 2015. A laboratory experiment on the behaviour of soil-derived core and intact polar GDGTs in aquatic environments. Biogeosciences 12, 933–943. https://doi.org/10.5194/bg-12-933-2015

Peterse, F., van der Meer, J., Schouten, S., Weijers, J.W.H., Fierer, N., Jackson, R.B., Kim, J.-H., Sinninghe Damsté, J.S., 2012. Revised calibration of the MBT–CBT paleotemperature proxy based on branched tetraether membrane lipids in surface soils. Geochimica et Cosmochimica Acta 96, 215–229. https://doi.org/10.1016/j.gca.2012.08.011

Revel, M., Colin, C., Bernasconi, S., Combourieu-Nebout, N., Ducassou, E., Grousset, F.E., Rolland, Y., Migeon, S., Bosch, D., Brunet, P., Zhao, Y., Mascle, J., 2014. 21,000 Years of Ethiopian African monsoon variability recorded in sediments of the western Nile deep-sea fan. Regional Environmental Change 14, 1685–1696. https://doi.org/10.1007/s10113-014-0588-x

Revel, M., Ducassou, E., Grousset, F.E., Bernasconi, S.M., Migeon, S., Revillon, S., Mascle, J., Murat, A., Zaragosi, S., Bosch, D., 2010. 100,000 Years of African monsoon variability recorded in sediments of the Nile margin. Quaternary Science Reviews 29, 1342–1362. https://doi.org/10.1016/j.quascirev.2010.02.006

Revel, M., Ducassou, E., Skonieczny, C., Colin, C., Bastian, L., Bosch, D., Migeon, S., Mascle, J., 2015. 20,000 years of Nile River dynamics and environmental changes in the Nile catchment area as inferred from Nile upper continental slope sediments. Quaternary Science Reviews 130, 200–221. https://doi.org/10.1016/j.quascirev.2015.10.030

Rochette, P., Tamrat, E., Féraud, G., Pik, R., Courtillot, V., Ketefo, E., Coulon, C., Hoffmann, C., Vandamme, D., Yirgu, G., 1998. Magnetostratigraphy and timing of the Oligocene Ethiopian traps. Earth and Planetary Science Letters 164, 497–510. https://doi.org/10.1016/S0012-821X(98)00241-6

Rohling, E.J., Grant, K., Bolshaw, M., Roberts, A.P., Siddall, M., Hemleben, Ch., Kucera, M., 2009. Antarctic temperature and global sea level closely coupled over the past five glacial cycles. Nature Geoscience 2, 500.

Rohling, E.J., Marino, G., Grant, K.M., 2015. Mediterranean climate and oceanography, and the periodic development of anoxic events (sapropels). Earth-Science Reviews 143, 62–97. https://doi.org/10.1016/j.earscirev.2015.01.008

Rossignol-Strick, M., Nesteroff, W., Olive, P., Vergnaud-Grazzini, C., 1982. After the deluge: Mediterranean stagnation and sapropel formation. Nature 295, 105–110. https://doi.org/10.1038/295105a0

Sanchi, L., Ménot, G., Bard, E., 2013. An automated purification method for archaeal and bacterial tetraethers in soils and sediments. Organic Geochemistry 54, 83–90. https://doi.org/10.1016/j.orggeochem.2012.10.005

Schefuß, E., Schouten, S., Schneider, R.R., 2005. Climatic controls on central African hydrology during the past 20,000 years. Nature 437, 1003–1006.

Scheuvens, D., Schütz, L., Kandler, K., Ebert, M., Weinbruch, S., 2013. Bulk composition of northern African dust and its source sediments — A compilation. Earth-Science Reviews 116,

170–194. https://doi.org/10.1016/j.earscirev.2012.08.005

Schouten, S., Hopmans, E.C., Rosell-Melé, A., Pearson, A., Adam, P., Bauersachs, T., Bard, E., Bernasconi, S.M., Bianchi, T.S., Brocks, J.J., Carlson, L.T., Castañeda, I.S., Derenne, S., Selver, A.D., Dutta, K., Eglinton, T., Fosse, C., Galy, V., Grice, K., Hinrichs, K.-U., Huang, Y., Huguet, A., Huguet, C., Hurley, S., Ingalls, A., Jia, G., Keely, B., Knappy, C., Kondo, M., Krishnan, S., Lincoln, S., Lipp, J., Mangelsdorf, K., Martínez-García, A., Ménot, G., Mets, A., Mollenhauer, G., Ohkouchi, N., Ossebaar, J., Pagani, M., Pancost, R.D., Pearson, E.J., Peterse, F., Reichart, G.-J., Schaeffer, P., Schmitt, G., Schwark, L., Shah, S.R., Smith, R.W., Smittenberg, R.H., Summons, R.E., Takano, Y., Talbot, H.M., Taylor, K.W.R., Tarozo, R., Uchida, M., van Dongen, B.E., Van Mooy, B.A.S., Wang, J., Warren, C., Weijers, J.W.H., Werne, J.P., Woltering, M., Xie, S., Yamamoto, M., Yang, H., Zhang, C.L., Zhang, Y., Zhao, M., Damsté, J.S.S., 2013. An interlaboratory study of TEX86 and BIT analysis of sediments, extracts, and standard mixtures. Geochem. Geophys. Geosyst. 14, 5263–5285. https://doi.org/10.1002/2013GC004904

Schouten, S., Hopmans, E.C., van der Meer, J., Mets, A., Bard, E., Bianchi, T.S., Diefendorf, A., Escala, M., Freeman, K.H., Furukawa, Y., Huguet, C., Ingalls, A., Ménot, G., Nederbragt, A.J., Oba, M., Pearson, A., Pearson, E.J., Rosell-Melé, A., Schaeffer, Shah, S.R., Shanahan, T.M., Smith, R.W., Smittenberg, R., Talbot, H.M., Uchida, M., Van Mooy, Be.A.S., Yamamoto, M., Zhang, Z., Sinninghe Damsté, J.S., 2009. An interlaboratory study of TEX86 and BIT analysis using high performance liquid chromatography/mass spectrometry. Geochem. Geophys. Geosyst 10. https://doi.org/doi:10.1029/2008GC002221

Schüler, L., Hemp, A., Zech, W., Behling, H., 2012. Vegetation, climate and fire-dynamics in East Africa inferred from the Maundi crater pollen record from Mt Kilimanjaro during the last glacial–interglacial cycle. Quaternary Science Reviews 39, 1–13. https://doi.org/10.1016/j.quascirev.2012.02.003

SCRP, 2000. SCRP (Soil Conservation Reserve Program) Area of Anjeni, Gojam, Ethiopia: Long-term monitoring of the agricultural environment 1984–1994, in: Soil Erosion and Conservation Database, Soil Conservation Research Programme. Centre for Development and Environment in association with the Ministry of Agriculture, Ethiopia, Berne, Switzerland.

Shanahan, T.M., McKay, N.P., Hughen, K.A., Overpeck, J.T., Otto-Bliesner, B., Heil, C.W.,

King, J., Scholz, C.A., Peck, J., 2015. The time-transgressive termination of the African Humid Period. Nature Geosci 8, 140–144.

Singarayer, J.S., Burrough, S.L., 2015. Interhemispheric dynamics of the African rainbelt during the late Quaternary. Quaternary Science Reviews 124, 48–67. https://doi.org/10.1016/j.quascirev.2015.06.021

Sinninghe Damsté, J.S., 2016. Spatial heterogeneity of sources of branched tetraethers in shelf systems: The geochemistry of tetraethers in the Berau River delta (Kalimantan, Indonesia). Geochimica et Cosmochimica Acta 186, 13–31. https://doi.org/10.1016/j.gca.2016.04.033

Sinninghe Damsté, J.S., Hopmans, E.C., Schouten, S., van Duin, A.C.T., Geenevasen, J.A.J., 2002. Crenarchaeol: the characteristic core glycerol diphytanyl glycerol tetraether membrane lipid of cosmopolitan pelagic crenarchaeota. J. Lipid Res. 43, 1641–1651.

Skonieczny, C., Paillou, P., Bory, A., Bayon, G., Biscara, L., Crosta, X., Eynaud, F., Malaizé, B., Revel, M., Aleman, N., Barusseau, J.-P., Vernet, R., Lopez, S., Grousset, F., 2015. African humid periods triggered the reactivation of a large river system in Western Sahara 6, 8751.

Smith, R.W., Bianchi, T.S., Savage, C., 2010. Comparison of lignin phenols and branched/isoprenoid tetraethers (BIT index) as indices of terrestrial organic matter in Doubtful Sound, Fiordland, New Zealand. Organic Geochemistry 41, 281–290. https://doi.org/10.1016/j.orggeochem.2009.10.009

Soulet, G., Ménot, G., Bayon, G., Rostek, F., Ponzevera, E., Toucanne, S., Lericolais, G., Bard, E., 2013. Abrupt drainage cycles of the Fennoscandian Ice Sheet. Proceedings of the National Academy of Sciences 110, 6682–6687. https://doi.org/10.1073/pnas.1214676110

Tachikawa, K., Vidal, L., Cornuault, M., Garcia, M., Pothin, A., Sonzogni, C., Bard, E., Menot, G., Revel, M., 2015. Eastern Mediterranean Sea circulation inferred from the conditions of S1 sapropel deposition. Climate of the Past 11, 855–867. https://doi.org/10.5194/cp-11-855-2015

Tebebu, T.Y., Abiy, A.Z., Zegeye, A.D., Dahlke, H.E., Easton, Z.M., Tilahun, S.A., Collick, A.S., Kidnau, S., Moges, S., Dadgari, F., Steenhuis, T.S., 2010. Surface and subsurface flow effect on permanent gully formation and upland erosion near Lake Tana in the northern highlands of Ethiopia. Hydrology and Earth System Sciences 14, 2207–2217.

https://doi.org/10.5194/hess-14-2207-2010

Thomson, J., Croudace, I.W., Rothwell, R.G., 2006. A geochemical application of the ITRAX scanner to a sediment core containing eastern Mediterranean sapropel units. Geological Society, London, Special Publications 267, 65. https://doi.org/10.1144/GSL.SP.2006.267.01.05

Tierney, J.E., deMenocal, P.B., 2013. Abrupt Shifts in Horn of Africa Hydroclimate Since the Last Glacial Maximum. Science 342, 843–846.

Tierney, J.E., Russell, J.M., Eggermont, H., Hopmans, E.C., Verschuren, D., Sinninghe Damsté, J.S., 2010. Environmental controls on branched tetraether lipid distributions in tropical East African lake sediments. Geochemica and Cosmochimica Acta 74, 4902–4918.

Tierney, J.E., Russell, J.M., Huang, Y., Damsté, J.S.S., Hopmans, E.C., Cohen, A.S., 2008. Northern Hemisphere Controls on Tropical Southeast African Climate During the Past 60,000 Years. Science 322, 252. https://doi.org/10.1126/science.1160485

Tierney, J.E., Russell, J.M., Sinninghe Damsté, J.S., Huang, Y., Verschuren, D., 2011. Late Quaternary behavior of the East African monsoon and the importance of the Congo Air Boundary. Quaternary Science Reviews 30, 798–807. https://doi.org/10.1016/j.quascirev.2011.01.017

Trauth, M.H., Foerster, V., Junginger, A., Asrat, A., Lamb, H.F., Schaebitz, F., 2018. Abrupt or gradual? Change point analysis of the late Pleistocene–Holocene climate record from Chew Bahir, southern Ethiopia. Quaternary Research 90, 321–330. https://doi.org/10.1017/qua.2018.30

Tuenter, E., Weber, S.L., Hilgen, F.J., Lourens, L.J., 2003. The response of the African summer monsoon to remote and local forcing due to precession and obliquity. Global and Planetary Change 36, 219–235. https://doi.org/10.1016/S0921-8181(02)00196-0

Utida, G., 2016. Holocene paleoenvironmental and paleoclimatic variations in Rio Grande do Norte (NE Brazil) reconstructed from lake sediments and speleothems. University of Sao Paulo.

Vadsaria, T., Ramstein, G., Dutay, J.-C., Li, L., Ayache, M., Richon, C., 2019. Simulating the

Occurrence of the Last Sapropel Event (S1): Mediterranean Basin Ocean Dynamics Simulations Using Nd Isotopic Composition Modeling. Paleoceanography and Paleoclimatology 34, 237–251. https://doi.org/10.1029/2019PA003566

Verschuren, D., Sinninghe Damste, J.S., Moernaut, J., Kristen, I., Blaauw, M., Fagot, M., Haug, G.H., members, C. project, 2009. Half-precessional dynamics of monsoon rainfall near the East African Equator. Nature 462, 637–641. https://doi.org/doi:10.1038

Viste, E., Sorteberg, A., 2013. The effect of moisture transport variability on Ethiopian summer precipitation. International Journal of Climatology 33, 3106–3123. https://doi.org/10.1002/joc.3566

Warden, L., Kim, J.-H., Zell, C., Vis, G.-J., de Stigter, H., Bonnin, J., Sinninghe Damsté, J.S., 2016. Examining the provenance of branched GDGTs in the Tagus River drainage basin and its outflow into the Atlantic Ocean over the Holocene to determine their usefulness for paleoclimate applications. Biogeosciences 13, 5719–5738. https://doi.org/10.5194/bg-13-5719-2016

Weijers, J., Schouten, S., van den Donker, J.C., Hopmans, E.C., Sinninghe Damste, J.S., 2007. Environmental controls on bacterial tetraether membrane lipid distribution in soils. Geochimica et Cosmochimica Acta 71, 703–713.

Weijers, J.W.H., Schouten, S., Spaargaren, O.C., Sinninghe Damsté, J.S., 2006. Occurrence and distribution of tetraether membrane lipids in soils: Implications for the use of the TEX86 proxy and the BIT index. Organic Geochemistry 37, 1680–1693.

Weldeab, S., Emeis, K.-C., Hemleben, C., Vennemann, T.W., Schulz, H., 2002. Sr and Nd isotope composition of Late Pleistocene sapropels and nonsapropelic sediments from the Eastern Mediterranean Sea: implications for detrital influx and climatic conditions in the source areas. Geochimica et Cosmochimica Acta 66, 3585–3598. https://doi.org/10.1016/S0016-7037(02)00954-7

Weldeab, S., Menke, V., Schmiedl, G., 2014. The pace of East African monsoon evolution during the Holocene. Geophys. Res. Lett. 41, 1724–1732. https://doi.org/10.1002/2014GL059361

Williams, M.A.J., Usai, D., Salvatori, S., Williams, F.M., Zerboni, A., Maritan, L., Linseele, V., 2015. Late Quaternary environments and prehistoric occupation in the lower White Nile valley, central Sudan. Quaternary Science Reviews 130, 72–88. https://doi.org/10.1016/j.quascirev.2015.03.007

Xiao, W., Wang, Y., Zhou, S., Hu, L., Yang, H., Xu, Y., 2016. Ubiquitous production of branched glycerol dialkyl glycerol tetraethers (brGDGTs) in global marine environments: a new source indicator for brGDGTs. Biogeosciences 13, 5883–5894. https://doi.org/10.5194/bg-13-5883-2016

Zell, C., Kim, J.-H., Dorhout, D., Baas, M., Sinninghe Damsté, J.S., 2015. Sources and distributions of branched tetraether lipids and crenarchaeol along the Portuguese continental margin: Implications for the BIT index. Continental Shelf Research 96, 34–44. https://doi.org/10.1016/j.csr.2015.01.006

Zhao, Y., Liu, Z., Colin, C., Paterne, M., Siani, G., Cheng, X., Duchamp-Alphonse, S., Xie, X., 2011. Variations of the Nile suspended discharges during the last 1.75Myr. Palaeogeography, Palaeoclimatology, Palaeoecology 311, 230–241. https://doi.org/10.1016/j.palaeo.2011.09.001

Zhu, C., Weijers, J.W.H., Wagner, T., Pan, J.-Ming., Chen, J.-F., Pancost, R.D., 2011. Sources and distributions of tetraether lipids in surface sediments across a large river-dominated continental margin. Organic Geochemistry 42, 376–386. https://doi.org/10.1016/j.orggeochem.2011.02.002

Table 1. Chronological framework. A reservoir age of 400 years was used for correction, in agreement with the age of 370 ± 40 years obtained for a pre-bomb shell of *Muricopsis trunculus* collected in Alexandria (Goiran, 2001).

Depth (cm)	Lab code	Species	Corrected ^{14}C age (yr BP)	± 1 SD	Calibrated age (yr BP)	± 1 SD	References
0.5	SacA005001	*G. ruber alba*	1060	35	577	13	**This study**
2.5	**SacA31699**	***G. ruber alba***	**1695**	**30**	**1258**	**20**	(Revel et al., 2015)
5.5	SacA22673	*G. ruber alba*	2670	30	2325	19	(Revel et al., 2015)
10.5	SacA22674	*G. ruber alba*	3345	30	3113	49	(Revel et al., 2015)
13.5	SacA16511	*G. ruber alba*	4160	30	4121	37	(Revel et al., 2015)
22	SacA16513	*G. ruber alba*	5570	30	5925	17	(Revel et al., 2015)
23.5	SacA22675	*G. ruber alba*	5795	30	6255	20	(Revel et al., 2015)
25	SacA16514	*G. ruber alba*	6055	30	6436	30	(Revel et al., 2015)
29.5	SacA005003	*G. ruber alba*	6415	50	6852	61	(Revel et al., 2015)
34.5	**SacA31700**	***G. ruber alba***	**6900**	**30**	**7430**	**15**	**This study**
65	SacA10935	*G. ruber alba*	7945	30	8371	19	(Revel et al., 2015)
70	SacA11797	*G. ruber alba*	8010	30	8403	15	(Revel et al., 2015)
95	SacA11798	*G. ruber alba*	8330	30	8712	68	(Revel et al., 2015)
102	SacA11799	*G. ruber alba*	8385	30	8891	30	(Revel et al., 2015)
120	SacA11800	*G. ruber alba*	8520	30	9068	19	(Revel et al., 2015)
205.5	SacA10936	*G. ruber alba*	9185	35	9784	49	(Revel et al., 2015)
274	SacA16516	*G. ruber alba*	10,835	40	12,282	58	(Revel et al., 2015)
286	SacA16517	*G. ruber alba*	11,495	40	12,982	69	(Revel et al., 2015)
293.5	SacA10937	*G. ruber alba*	12,795	45	14,127	71	(Revel et al., 2015)
298	**SacA31702**	***Bulk planktic***	**13,630**	**60**	**15,280**	**108**	**This study**
300.5	**SacA31703**	***Bulk planktic***	**15,590**	**60**	**17,989**	**91**	**This study**
303	SacA16518	*G. ruber alba*	17,470	70	20,588	104	(Revel et al., 2015)

Table 2. Organic sample flow-through.

MS27PT Number of samples	**TLE extraction**	**TLE separation**	**GDGT-analysis**	**2nd GDGT-analysis for methyl separation**
159	**at LOCEAN (Sorbonne Universités)** based on Utida (2016) ultrasonic bath (DCM/MeOH, 3:1)	**at LOCEAN (Sorbonne Universités)** based on Utida (2016) Silica gel chromatography F1: 4 mL hexane F2: 2 mL hexane/ethyl acetate (95:5) **F3: 2 mL hexane/ethyl acetate (90:10)** **F4: 4 mL hexane/ethyl acetate (70:30)** F5: 4 mL DCM/MeOH (50:50)	**at CEREGE** based on Ménot and Bard (2012) and Sanchi et al. (2013)	60 samples **at CEREGE** based on Davtian et al., (2018)
57 (additional sampling every cm for the interval 207–303 cm)	**at CEREGE** based on Ménot and Bard (2012) Accelerated Solvent Extractor (Dionex ASE-200, DCM/MeOH 9:1)	**at CEREGE** based on Sanchi et al. (2013) F1: 4 mL hexane/DCM (50:50) **F2: 6 mL MeOH/DCM (50:50)**		

Figure 1. Geological context of the Nile basin. A: Hydrological context of North Africa and the present-day active Nile watershed (modified from Skonieczny et al., 2015). Three main sources of particles deposited into the Nile deep-sea fan are shown: the orange area represents the main source of aeolian dust coming from the Sahara Desert due to south-easterly winds (Scheuvens et al., 2013). Nd isotopic compositions of aerosol samples from Libya and Egypt (Precambrian basement) is from (Grousset and Biscaye, 2005). The Blue and Atbara Nile tributaries drain the Ethiopian Traps (in purple) composed by Cenozoic basalt (Rochette et al., 1998). The equatorial tributary of the Nile drains the Precambrian Craton (in green) from Victoria lake to Khartoum composed mainly by Precambrian metamorphic rocks. The outcrops of Ethiopian Traps and Precambrian Craton provide sediments characterised by εNd values of 0 and -30, respectively (Garzanti et al., 2015). The seasonal positions of the Intertropical Covergence Zone – ITCZ – as well as of the Congo Air Boundary – CAB – over Africa are also represented in black and grey dotted lines, respectively. The main moisture patterns over the Nile watershed are illustrated by light blue arrows, their positions are approximated and are derived from (Viste and Sorteberg, 2013). Locations of sediment cores and lakes discussed in the regional synthesis are also reported. **B**: Bathymetric map of the Nile margin showing the specific location of core MS27PT used in this study (red star). Also shown the cores from the Levantine basin: P362/2-33 (Blanchet et al., 2013); MS21PC and PS009PC (Hennekam et al., 2014), SL112 (Weldeab et al., 2014) and GeoB 7702-3 (Castaneda et al., 2010). **C:** Comparison of the sedimentation rate (cm/ka) of these six cores, with different x-axis values in each case.

Figure 2. Geochemical records in core MS27PT in the Nile deep-sea fan. A. εNd values; open symbols correspond to the present study, while closed symbols represent data previously published (Revel et al., 2015, 2014). Variations of relative sea level (Rohling et al., 2009) are

plotted **B.** ΣIIIa/ΣIIa ratio (reversed axis) and 15°N insolation (Berger, 1981), **C.** BIT-index values. On panels **B** and **C**, closed symbols represent values measured with the the old chromatographic setting, open symbols represent samples remeasured with the 2D chromatographic method (cf. Methods); the sedimentation rate expressed in cm/ka is plotted. **D.** Fluxes of crenarchaeol (blue shaded area) and brGDGTs (greenish shaded area). **E.** Manganese percentage (pink symbols, this study) and sulfur percentage (grey open symbols, (Revel et al., 2010)) and S/Cl intensity in number of counts based on XRF core scanner (grey line, (Revel et al., 2010)). The red triangles refer to ^{14}C dates (Revel et al., 2015, 2014, 2010). **F.** Simplified sedimentary log of core MS27PT after Ducassou et al. (2008) and Revel et al. (2014). Grey shaded areas correspond to "anoxic" layers as indicated by the sulfur content. The red section stands for the laminated section of the sedimentary sequence (name clastic mud beds in Ducassou et al., (2008). These laminations are interpreted as very dense suspension rich (hyperpycnal) flows formed by reconcentration of particle-laden seasonal Nile flood plumes in the water column, which were subsequently deposited on the sea floor (Blanchet et al., 2013; Ducassou et al., 2008). These laminatations indicate the absence of bioturbation by benthic faunal organisms because of increased of density stratification of the eastern Mediterranean.

Figure 3. Significance of the ΣIIIa/ΣIIa ratio in the Nile delta as a proxy of the terrigenous supply. **A.** Cross plot of BIT-index and ΣIIIa/ΣIIa ratio. Dataset of core MS27PT (large circles, colors refer to time interval of deposition) compared with data of Davtian et al. (2016) and Xiao et al. (2016) (small symbols; blue and brown colors refer to open ocean and soil samples, respectively). The closed brown symbols refer to soil samples from the previously cited database collected in Intertropical areas worldwide. The orange and blue lines refer to the 0.59 and 0.92 values defined as the upper limit for soil ΣIIIa/ΣIIa values and

the lower limit for open ocean values, respectively (Xiao et al., 2016). **B.** Enlargement of the ΣIIIa/ΣIIa interval from 0.1 to 0.5, which contains most of the data from core MS27PT. **C.** Cross plot of the fractional abundance of the tetramethylated brGDGTs versus the pentamethylated brGDGTs. Large circles refer to the MS27PT dataset and the symbol colors correspond to the ΣIIIa/ΣIIa ratio of the samples. Small symbols refer to published datasets of soil, sediment and suspended particulate matter samples (open black circles – compilation of Naafs et al. (2017), open brown circles (De Jonge et al., 2016, 2015), blue triangles (Warden et al., 2016) and green triangles (Sinninghe Damsté, 2016)). Similarly, on Panel A., the brown closed symbols refer to soil samples, from the world database, collected in the tropical realm.

Figure 4. Regional significance of the Nile deep-sea fan sedimentary records at the scale of the Eastern Mediterranean basin. A. Summer 15°N Insolation (Berger, 1981) and relative sea level (Rohling et al., 2009) curves. Comparison of the BIT-index curves available on a west-east local transect: **B.** MS27PT (this study), **C.** P362/2-33 (Blanchet et al., 2015) and **D.** GeoB7702-3 (Castaneda et al., 2010). Similar comparison for the few εNd records: **E.** MS27PT (this study) and **F.** P362/2-33 *(Blanchet et al., 2014).*

Figure 5. Hydrological changes in Africa through the last 20 ka. A. ΣIIIa/ΣIIa (reversed axis) and BIT-index from core MS27PT. East African precipitation records: **B.** δD_{wax} from Lake Tana (reversed axis, Costa et al., 2014) and insolation curve (Berger, 1981) and **C.** δD_{wax} from Lake Tanganyika (reversed axis, Tierney et al., 2008). West Africa precipitation records: **D.** Lake-level history of Lake Chad (Armitage et al., 2015). Closed and open symbols are for Lake Chad and the Bodélé Basin, respectively. **E.** δD_{wax} from Lake Bosumtwi (Shanahan et al., 2015) and from Lake Barombi Mbo (open symbols, Garcin et al., 2018) (reversed axis in both cases) and **F.** δD_{wax} from the Congo deep-sea fan, GeoB 6518-1

(reversed axis, Schefuß et al., 2005). Shaded green area underlines the African Humid Period in its historical definition (5–11 ka,, Gasse, 2000)) and grey areas underline North Hemisphere climatic events, H1 and YD stand for Heinrich Event 1 and Younger Dryas, respectively.

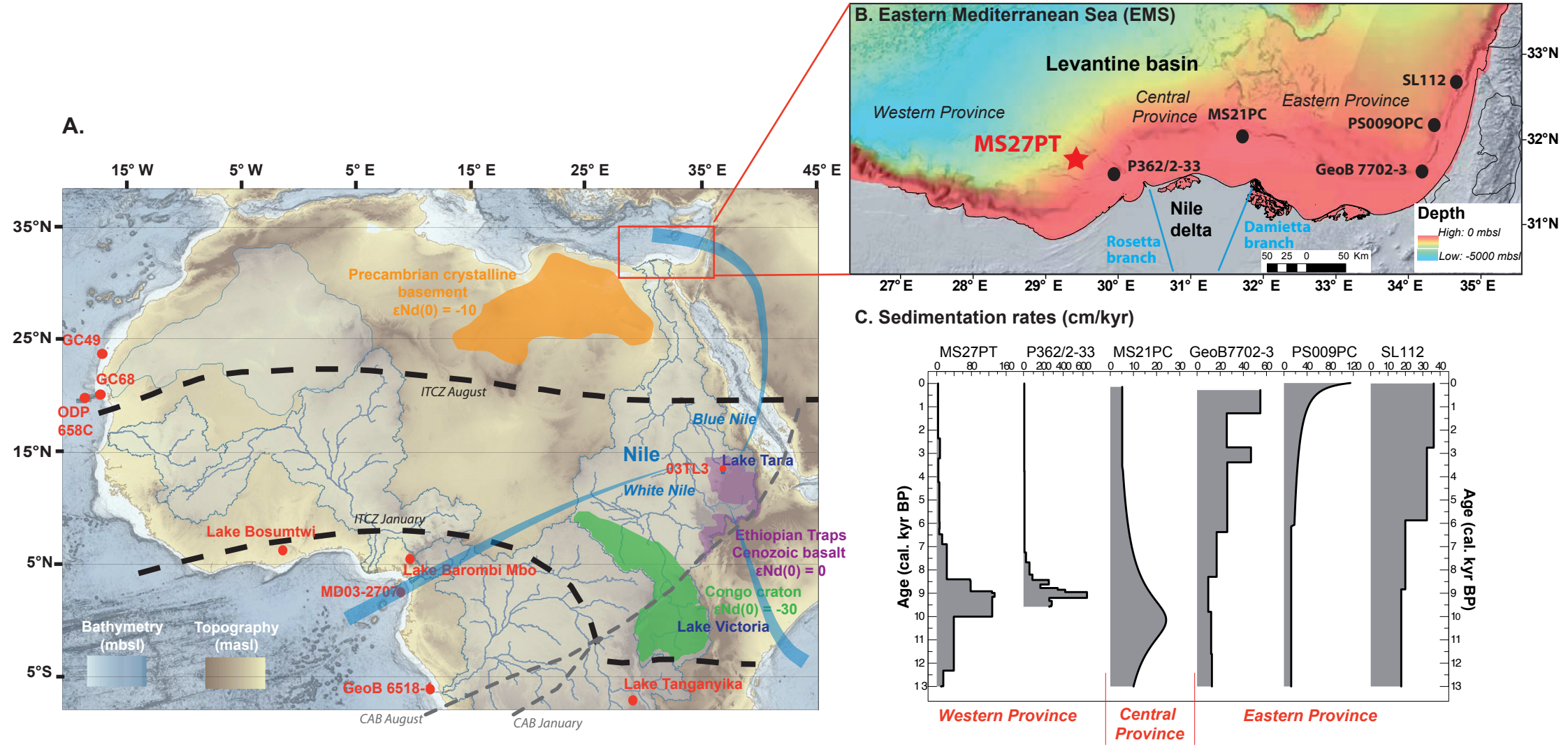
A.
15° W
5° W
5° E
15° E
25° E
35° E
45° E
35°N
25°N
15°N
5°N
5°S
GC49
GC68
ODP 658C
Precambrian crystalline basement εNd(0) = -10
ITCZ August
ITCZ January
Blue Nile
Nile
White Nile
03TL3
Lake Tana
Lake Bosumtwi
Lake Barombi Mbo
MD03-2707
Ethiopian Traps Cenozoic basalt εNd(0) = 0
Congo craton εNd(0) = -30
Lake Victoria
GeoB 6518-1
Lake Tanganyika
CAB August
CAB January
Bathymetry (mbsl)
Topography (masl)
B. Eastern Mediterranean Sea (EMS)
Levantine basin
Western Province
Central Province
Eastern Province
MS27PT
MS21PC
P362/2-33
PS009OPC
SL112
GeoB 7702-3
Nile delta
Rosetta branch
Damietta branch
Depth
High: 0 mbsl
Low: -5000 mbsl
50 25 0 50 Km
27° E
28° E
29° E
30° E
31° E
32° E
33° E
34° E
35° E
33°N
32°N
31°N
C. Sedimentation rates (cm/kyr)
MS27PT
P362/2-33
MS21PC
GeoB7702-3
PS009PC
SL112
Age (cal. kyr BP)
Western Province
Central Province
Eastern Province

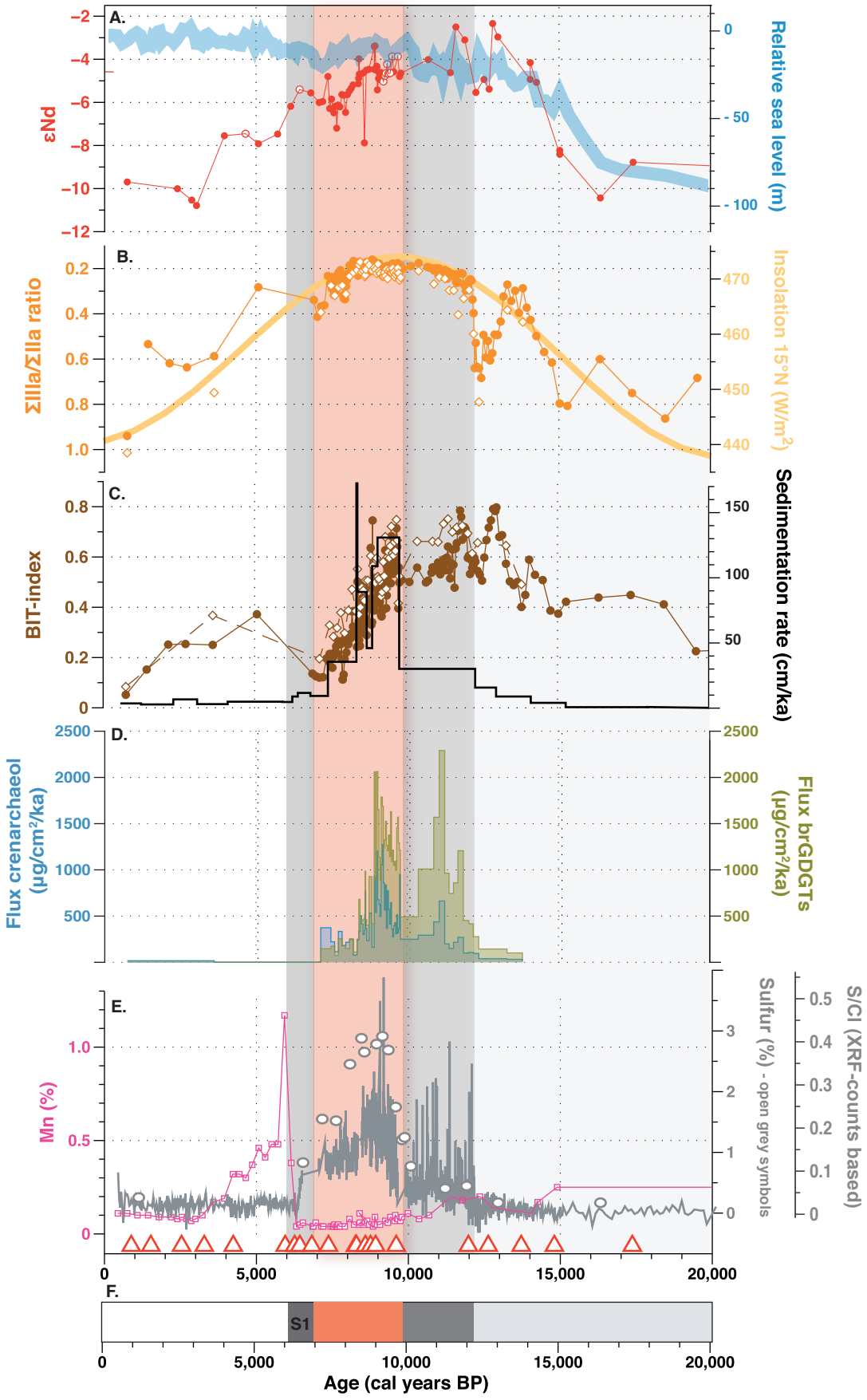
A.
εNd
Relative sea level (m)
B.
ΣIIIa/ΣIIa ratio
Insolation 15°N (W/m²)
C.
BIT-index
Sedimentation rate (cm/ka)
D.
Flux crenarchaeol (µg/cm²/ka)
Flux brGDGTs (µg/cm²/ka)
E.
Mn (%)
Sulfur (%) - open grey symbols
S/Cl (XRF-counts based)
F.
S1
Age (cal years BP)

Figure 2

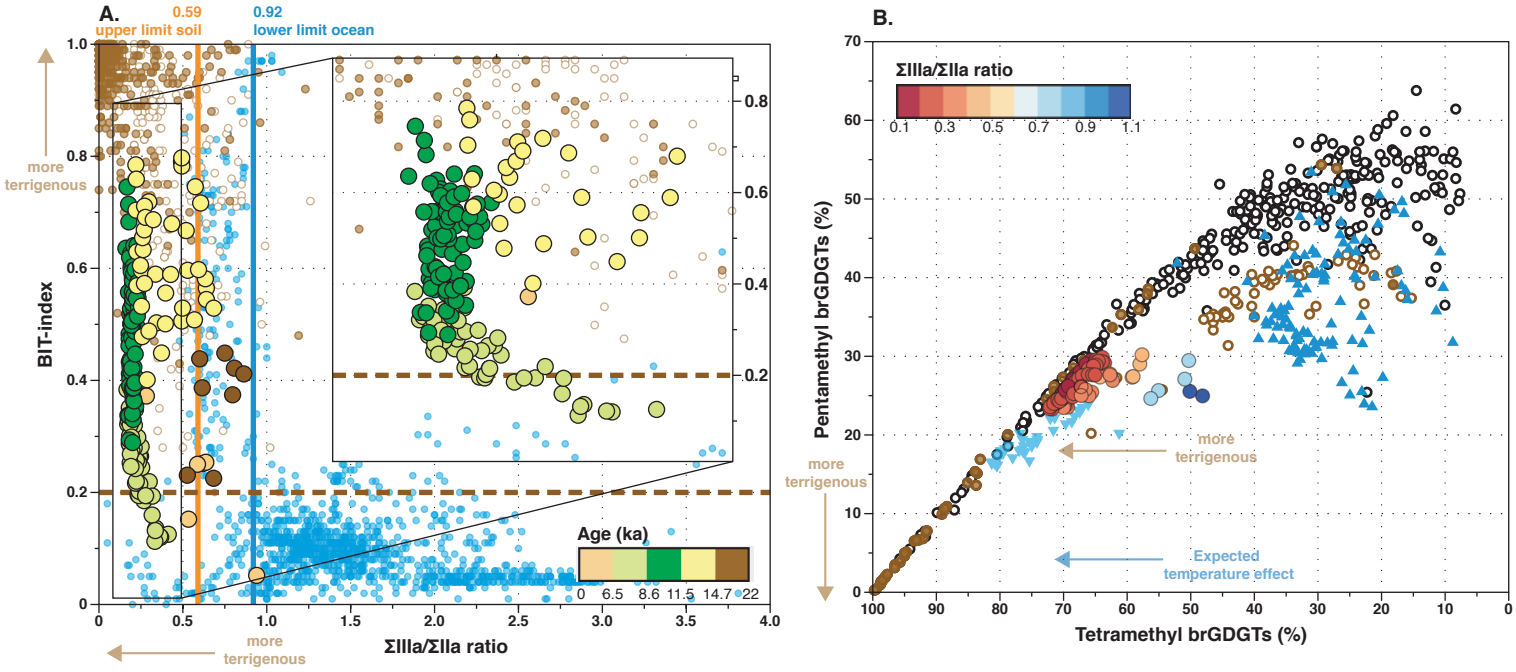
A.
0.59
upper limit soil
0.92
lower limit ocean
more terrigenous
BIT-index
Age (ka)
0 6.5 8.6 11.5 14.7 22
ΣIIIa/ΣIIa ratio
more terrigenous
B.
ΣIIIa/ΣIIa ratio
0.1 0.3 0.5 0.7 0.9 1.1
Pentamethyl brGDGTs (%)
more terrigenous
more terrigenous
Expected temperature effect
Tetramethyl brGDGTs (%)

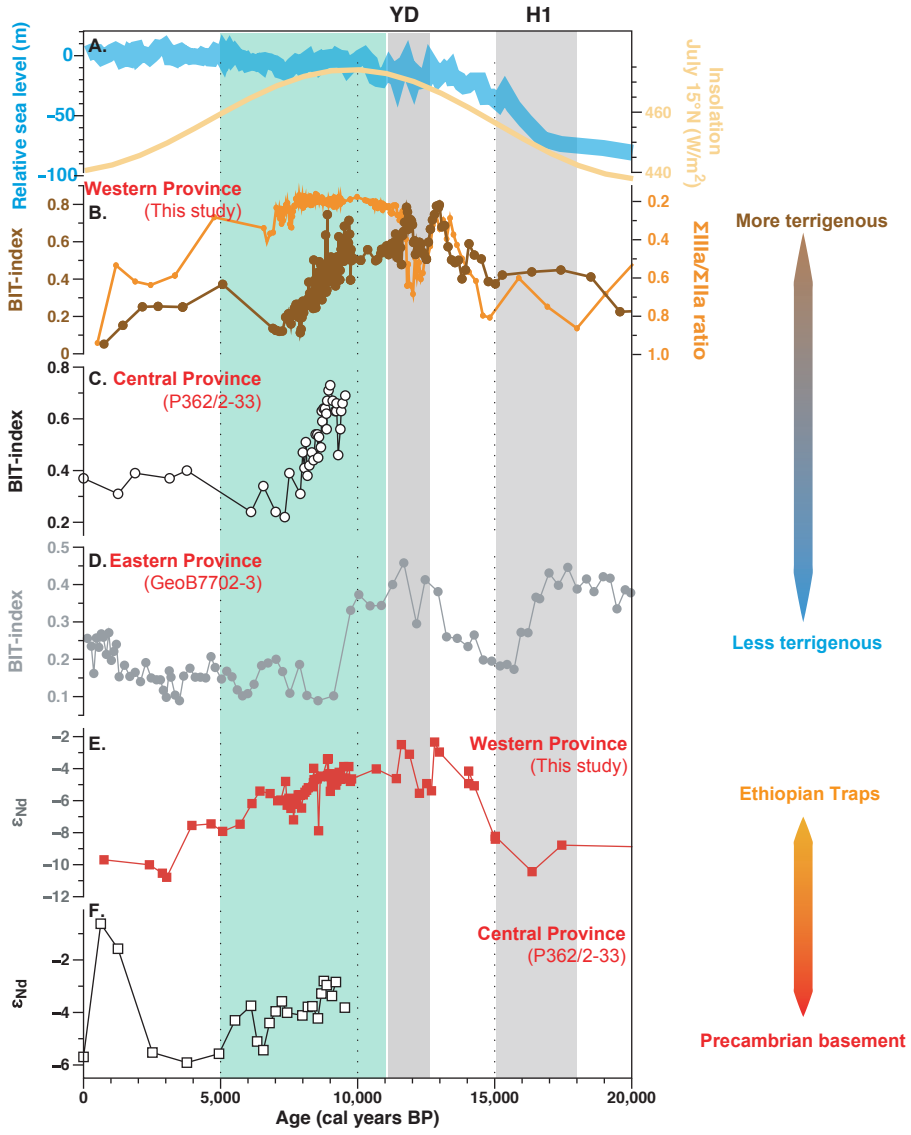
YD
H1
A.
Relative sea level (m)
0
-50
-100
Insolation July 15°N (W/m²)
460
440
Western Province
(This study)
B.
BIT-index
0.8
0.6
0.4
0.2
0
ΣIIIa/ΣIIa ratio
0.2
0.4
0.6
0.8
1.0
C. Central Province
(P362/2-33)
BIT-index
0.8
0.6
0.4
0.2
D. Eastern Province
(GeoB7702-3)
BIT-index
0.5
0.4
0.3
0.2
0.1
E.
Western Province
(This study)
εNd
-2
-4
-6
-8
-10
-12
F.
Central Province
(P362/2-33)
εNd
-2
-4
-6
0
5,000
10,000
15,000
20,000
Age (cal years BP)
More terrigenous
Less terrigenous
Ethiopian Traps
Precambrian basement

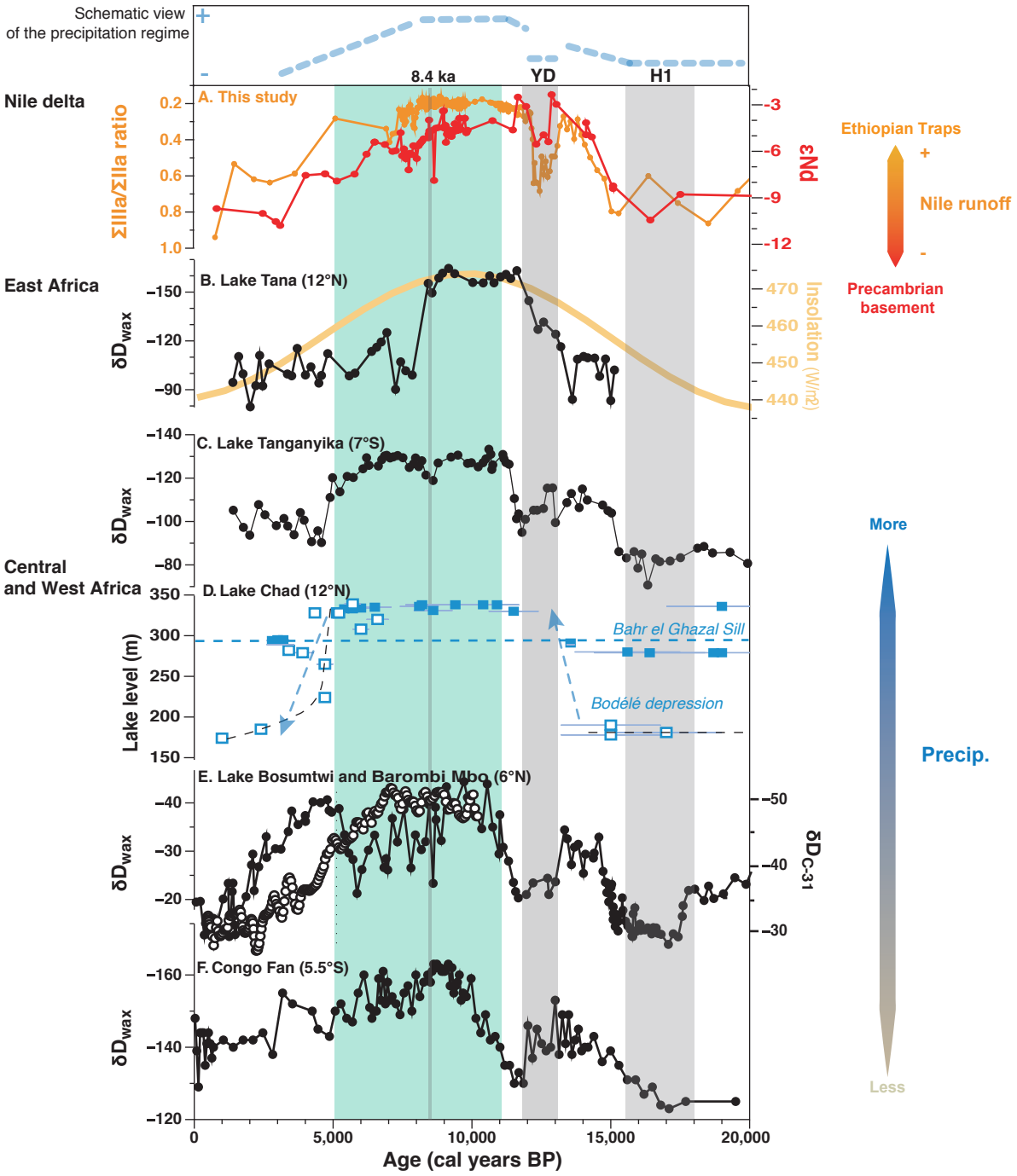
Schematic view
of the precipitation regime
+
-
8.4 ka
YD
H1
Nile delta
A. This study
ΣIIIa/ΣIIa ratio
0.2
0.4
0.6
0.8
1.0
εNd
-3
-6
-9
-12
Ethiopian Traps
+
Nile runoff
-
Precambrian
basement
East Africa
B. Lake Tana (12°N)
δDwax
−150
−120
−90
Insolation (W/m2)
470
460
450
440
C. Lake Tanganyika (7°S)
−140
−120
−100
−80
Central
and West Africa
D. Lake Chad (12°N)
Lake level (m)
350
300
250
200
150
Bahr el Ghazal Sill
Bodélé depression
More
Precip.
Less
E. Lake Bosumtwi and Barombi Mbo (6°N)
−40
−30
−20
δDC-31
−50
−40
−30
F. Congo Fan (5.5°S)
−160
−140
−120
0
5,000
10,000
15,000
20,000
Age (cal years BP)